



**Modelling of Two-Phase Critical Flow In Steam Generator Tube Guillotine Rupture
Scenario With Apros for the C-FLOW Separate-Effect-Test Facility**

Lappeenranta–Lahti University of Technology LUT

Master's thesis

2023

Andrei Zaitsev

Examiners: Professor, Juhani Hyvärinen

Lauri Pyy, M. Sc (Tech)

ABSTRACT

Lappeenranta–Lahti University of Technology LUT

LUT School of Energy Systems

Degree Program in Nuclear Energy Engineering

Andrei Zaitsev

Modelling of Two-Phase Critical Flow In Steam Generator Tube Guillotine Rupture Scenario With Apros for the C-FLOW Separate-Effect-Test Facility

Master's thesis

2023

90 pages, 47 figures, 1 table.

Examiners: Professor D.Sc. (Tech) Juhani Hyvärinen and M. Sc (Tech) Lauri Pyy

Supervisor: D. Sc (Tech) Giteshkumar Patel, M.Sc. (Tech) Lauri Pyy & M.Sc. (Tech) Virpi Kouhia

Keywords: critical flow, two-phase critical flow, TPCF, choked flow, primary-to-secondary leak, PRISE, Apros, Separate-effect-test facility, SET, Steam generator tube, C-FLOW, SAFER2028

The purpose of this master's thesis is to investigate two-phase critical mass flow rate in a separate-effect-test facility proposed to be built in LUT University's Nuclear laboratory under C-FLOW project funded by SAFER2028 National Research Programme. The facility focuses on critical flow discharges in a primary-to-secondary leak scenario when steam generator tube undergoes a guillotine break. For this purpose, a test facility is being built, consisting of an upstream pressure vessel, a larger diameter measuring pipe with volume flow measurement and shut-off valve, tube for discharging steam/water mixture to atmosphere with different length-to-diameter ratios. The main idea of the facility is to use different L/D ratio discharge tubes and to examine effects of the very long upstream discharge tube on to critical mass flow rate. L/D ratio larger than 302 has not been found in the literary and the separate-effect-test in C-FLOW will broaden this with representative steam generator tube sizes of VVER-440 and EPR. This work includes a theoretical examination of critical mass flow in terms of mathematical models. Different mathematical models are examined and how they describe one- and two-phase critical mass flow rate. The work consists of a review of the most important SETs used in the prior studies and few examples of newer experimental work that can be considered state-of-the-art. Additionally, a simulation model using the Apros system code is created to model the test facility. By using the results obtained from the simulation, it is possible to find out the critical pressure ratio where the two-phase critical flow conditions are met for tubes with different L/D ratios. Furthermore, the simulation results provide valuable insights into various critical parameters, including void fraction along the discharge tube, void fraction at the end of the discharge tubes, pressures at the end of discharge tubes, mass flow rates, and velocities for both phases. These comprehensive findings enhance our understanding of the system's behaviour and aid in optimizing its performance, ensuring safer and more efficient operation.

ACKNOWLEDGEMENTS

To begin with, I would like to express my appreciation to my supervisor, M. Sc (Tech) Lauri Pyy, for his guidance and support throughout the entire journey of my thesis. I am grateful for his mentorship provided me during this project.

I would also like to extend my gratitude to D.Sc. (Tech) Giteshkumar Patel. His insights and feedback have been immensely valuable.

Furthermore, I would like to express my gratitude to M.Sc. (Tech) Virpi Kouhia, whose support and guidance have been important. Her knowledge and expertise in Apros code have enriched my understanding of the subject, and I am thankful for the opportunities she provided me to expand my horizons.

I would like to extend my sincere thanks to Prof. D.Sc. (Tech) Juhani Hyvärinen for his invaluable teachings and mentorship during my master's degree studies in Nuclear Engineering.

Finally, I wish to acknowledge my parents and my family for their support and encouragement throughout my studies.

Once again, I extend my deepest gratitude to all those mentioned above, as well as to the entire staff of the Nuclear Engineering department at Lappeenranta University of Technology (LUT). Their collective efforts and contributions have significantly enriched my academic journey, and I am honoured to have been a part of such an inspiring community.

Andrei Zaitsev, October 2023.

SYMBOLS AND ABBREVIATIONS

p	pressure	[Pa]
m	mass flow rate	[kg/s]
R	gas constant	[J/kg K]
T	temperature	[°C, K]
U	medium speed locally	[m/s]
a	local sound of speed	[m/s]
V	volume	[m ³]
v	specific volume	[m ³ /kg]
x	vapour content	[-]
h	enthalpy	[kJ/kg]
k	poisson's ratio	[-]
ρ	density	[kg/m ³]
A	area	[m ²]
G	mass flux	[kg/sm ²]
σ	surface tension	[N/m]
T	stress tensor	[Pa]
k	turbulent kinetic energy	[m ² /s ²]
u	velocity	[m/s]
t	time	[s]
P	space time averaged mixture pressure	[Pa]
s	entropy	[J/kgK]
L	length	[m]

D	diameter	[m]
τ_{Fg}	shear stress between the vapor layer and the wall	[Pa]
τ_{Ff}	shear stress between the liquid layer and the wall	[Pa]
τ_i	interfacial shear stress	[Pa]
P_{Fg}	portion of channel's perimeter covered with vapor	[-]
P_{Ff}	portion of channel's perimeter covered with liquid	[-]
P	perimeter	[m]
P	pressure	[Pa]
z	stream-wise coordinate	[-]
α	void fraction	[-]
Γ_{fg}	mass transfer rate	[kg/m ³ s]
g	gravitational acceleration	[m/s ²]
B	decay constant	[-]
ρ'	momentum density	[kgm/s]
$\bar{\rho}$	mixture density	[kg/m ³]

Subscripts

0	stagnation condition
c	critical
l	liquid
s	constant entropy
g	vapor

<i>t</i>	throat
<i>up</i>	upstream
<i>e</i>	equilibrium
<i>LT</i>	long tube's quality
<i>eq</i>	exit quality
<i>k</i>	liquid or gas
<i>i</i>	interface
<i>w</i>	wall
<i>F</i>	friction force
<i>Q</i>	heat flow
<i>va</i>	valve friction
<i>fl</i>	friction from form loss
<i>pu</i>	pump head
<i>n</i>	non-condensable

Abbreviations

SGTR	Steam generator tube rupture
PWR	Pressurized water reactor
LOCA	Loss of coolant accident
SCC	Stress-Corrosion Cracking
ECCS	Emergency core cooling system
TPCF	Two-phase critical flow
HEM	Homogeneous equilibrium model
SFM	Separated flow models.

Abbreviations

SET	Separate-effect-test facility.
CFT	Critical flow tests
PCV	Pressure control valve
FCV	Flow control valve
QOV	Quick-opening valve
DAS	Data acquisition system
LBB	Leak-before-break
VTT	VTT Technical Research Centre of Finland
TVO	Teollisuuden Voima Oy
CANDU	Canadian Deuterium Uranium Reactor

Table of contents

Abstract.....	2
Acknowledgements.....	3
Symbols and abbreviations.....	4
1 Introduction	10
1.1 Background	10
1.2 Motivation for the Thesis	12
2 Critical flow.....	13
2.1 Single-phase critical flow.....	14
2.2 Two-phase critical flow.....	16
2.3 Models of two-phase critical flow based on the Separated Flow Models.....	22
2.3.1 Critical mass flux according to Fauske’s relation.....	28
2.3.2 Critical mass flux according to Moody’s relation	29
2.3.3 Models of two-phase critical flow based on the Homogeneous Equilibrium Model (HEM)	31
2.4 Conclusions of two-phase critical flow models	34
3 State-of-the-art in two-phase critical flow modelling	35
3.1 Super Moby Dick	37
3.2 Marviken	39
3.3 Experimental study on a two-phase critical flow with a non-condensable gas at high pressure conditions.....	44
3.4 Experimental study of the critical flashing flow through a relief line: evidence of the double-choked flow phenomena	47
3.5 High-pressure water flow through narrow, sharp-edged tubes in a state of critical flow.....	51
3.6 A metastable jet model for leaks in steam generator tube.	55
3.7 A study of subcooled choked flow in real steam generator tube cracks.	59
3.8 Summary on the two-phase critical flow modelling	62
4 C-FLOW Separate-Effect-Test Facility.	63

4.1	Design of C-FLOW test facility	64
5	Apros simulation model of C-FLOW test facility for two-phase critical flow study...	66
5.1	Apros code	66
5.2	Simulation model	70
6	C-flow test facility Apros simulation results and analysis	72
7	Conclusion.....	83
	References.....	86

1 Introduction

This section reviews the reasons why studying critical flow is important and why understanding this phenomenon is crucial for the safety of a nuclear power plant. Additionally, the goals of this work will be discussed and methods to achieve them will be explored.

1.1 Background

When operating a nuclear power plant, it is crucial to take into account different potential accident scenarios. One of the critical accident scenarios in the design basis, considering nuclear safety, is the occurrence of a steam generator tube rupture (SGTR) (Nematollahi & Zare, 2008). Steam generators are heat exchangers responsible for converting water into steam on the secondary side using the heat generated by nuclear reactors. The steam generator tube inside a typical vertical steam generator is presented in Figure 1.

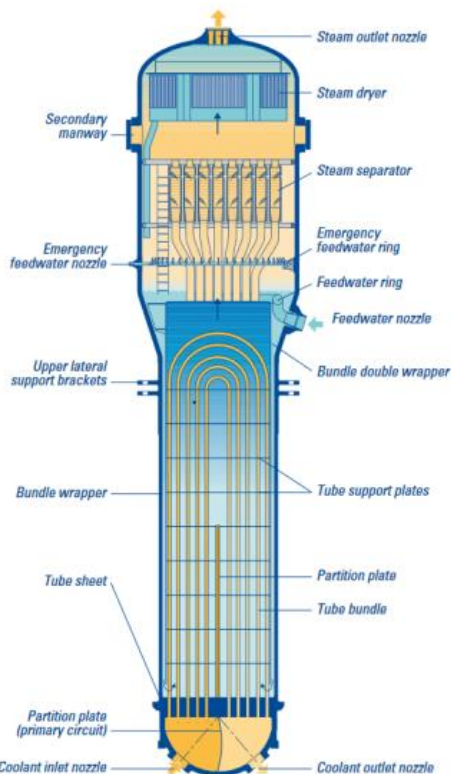


Figure 1: The sketch of steam generator in Olkiluoto 3 EPR. (TVO, 2010)

The integrity of the steam generator tube is very important as it acts as a radiation release boundary between the primary and secondary circuit and is designed to withstand high-pressure differences, such as 8.6 MPa in pressurised water reactor (PWR) during nuclear reactor operation. However, steam generator tubes are still susceptible subjected to the effects of corrosion and mechanical harm to some extent. When a corrosive environment, susceptible materials, and constant tensile stress combine, Stress-Corrosion Cracking (SCC) can occur, which is a significant mechanism leading to SGTR. The integrity of steam generator tubes is of utmost importance to prevent accidents involving the loss of coolant (LOCA) and SGTR. While both involve loss of coolant, it is vital to differentiate between the two scenarios, as they present distinct challenges. In such accident scenarios, the critical mass flow rate at the tube rupture plays a crucial role (Revankar & Riznic, 2019). SGTRs occur when a tube ruptures, leading to a comparatively slow loss of coolant. The leak area in such cases is relatively small, causing the coolant to end up in the secondary side rather than being discharged into the containment. Unlike a LOCA, where coolant remains inside the containment and can be recirculated back to the reactor, an SGTR results in permanent loss of coolant and prevents the possibility of recirculation. To minimize leak flow, the primary system can be depressurized, but it must be done cautiously to avoid reversing the flow, which could lead to undesirable dilution of the primary coolant boron concentration. The challenge in predicting the SGTR leak flow rates is effect of the potentially very long tube upstream of the break. The largest L/D ratios observed in some cases far exceed the limits of the current critical flow SET database, making accurate predictions challenging. To enhance the design of Emergency Core Cooling Systems (ECCS) and containment safety systems, it is essential to accurately calculate the discharging mass flow rate at the rupture point. Also, for the advanced reactor designs, which relate on to passive ECCS is important to predict accurately the two-phase critical flow (TPCF) (Lanfredini et al., 2020).

The development of a Two-Phase Critical Flow (TPCF) model is still necessary due to significant prediction errors in critical mass flow rate compared to steady-state benchmark experiments, as indicated by the FONESYS network. In their 2015 study, the FONESYS network focused on modelling critical flow rates using various system codes, and the relative error in predictions reached up to 40% when approaching saturation conditions. In highly subcooled situations, the prediction error was around 20% (Lanfredini, et al., 2020). This comparative analysis of different system codes regarding critical mass flow rate can be considered the current state-of-the-art in TPCF modelling. Furthermore, there is a need for

experiments with a large length-to-diameter (L/D) ratio since the most common steam generator tube ruptures occur in the immediate vicinity of the tube sheet or within the U-bend region. The L/D ratio is an important factor in assessing two-phase critical flow during tube rupture scenarios. It influences the flow regime transition, pressure drop, and flow stability, all of which are crucial for evaluating system behaviour. Steam generator tubes of EPR-type PWR's longest tube length is about 25300 mm, and the L/D ratio will be around 1500 (TVO,2010). The maximum L/D ratio for the VVER-440 is about 712 and for VVER-1200 is about 1064 (MacDonald et al., 1996). Experiments with an L/D ratio larger than 302 have not been found in a publicly available literature (Fraser & Abdelmessih, 2002). Considering similar tube rupture locations in the different types of steam generators means that there is a need for experiments with L/D ratios larger than 350, which is the U-bend distance in the VVER-440 steam generator.

For critical flow research purposes, LUT is planning and constructing a separate-effect-test facility (SET). The research work with the planned facility will focus on the PRISE leak situation where a guillotine break occurs in a steam generator tube. The primary aim of the project is to investigate critical flow parameters with different L/D ratios of heat exchanger steam generator tubes. According to the findings from the literature research, the suggested experimental setup represents a novel approach to investigating critical flow phenomena. This proposed test facility aims to enhance the current state of the critical mass flow rate database by incorporating a significantly larger length-to-diameter (L/D) ratio, along with representative tube diameters found in EPR and VVER-440 reactors.

1.2 Motivation for the Thesis

The work is aimed to make a preliminary study for critical flow research, with the motivation of studying leak flow rate to design the safety systems and accident management procedures, ensuring the plant can be brought to a safe state and maintained there. The work examines different mathematical models and how they describe critical mass flow rates in both single-phase and two-phase flow conditions. State-of-the-art research in the literature focusing on measurements and modelling of two-phase critical mass flow is also discussed. Also, a simulation model using the Apros system codes is created to model the test facility. By using the results obtained from the simulation, it is possible to have a preliminary prediction on

the critical pressure ratio where the two-phase critical flow conditions are met for tubes with different L/D ratios and upstream conditions. Other important parameters like variation of the discharge as function of time-dependent upstream condition can be investigated that can offer insights on how to conduct experiments in the facility in future.

2 Critical flow

Understanding the critical flow phenomena is crucial for assessing steam generator tube rupture events (SGTR) and loss of coolant accidents (LOCA). Therefore, it is crucial to understand the fundamental characteristics of a flow as a function of time, such as density, vapor and liquid velocity, and flow type (Sokolowski & Kozlowski, 2012). The critical flow, which is determined by the Mach number Eqs. (1), happens when the flow velocity matches local speed of sound:

$$M = \frac{U}{a} \quad (1)$$

where, U is medium speed locally [m/s]

a is local sound of speed [m/s]

When the Mach number get value $M < 1$ the flow is subcritical, $M = 1$ flow is critical and when $M > 1$ the flow is supersonic. Critical flow is sometimes referred to as choked flow. The underlying cause of choking is the loss of upstream acoustic signal propagation. Simply expressed, the greatest speed at which a compressible fluid may move from one area of higher pressure to another is known as the speed of sound (Sokolowski&Kozlowski, 2012).

The discharge from a tank via a pipe is shown in Figure 2, with p_0 and p_R standing for the pressures inside the tank and at the pipe's outlet, respectively (Sokolowski&Kozlowski, 2012). Only the stagnation parameters have any influence on the critical mass flow rate. Figure 2 presents how critical flow phenomena manifest itself.

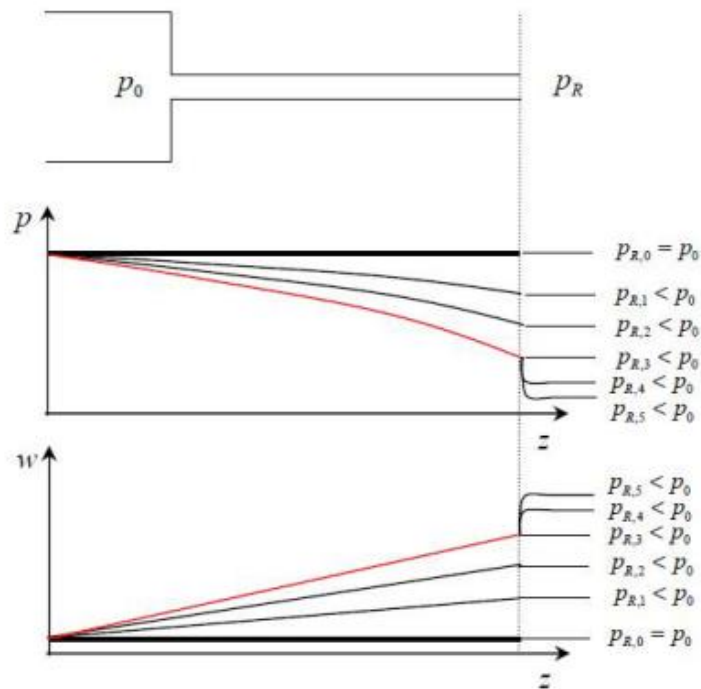


Figure 2: Behaviours of critical pressure and velocity (Sokolowski&Kozlowski, 2012).

It observed that the medium velocity increases as downstream pressure lowers. However, this velocity increase occurs only until a certain point where the process behaviour becomes unaffected by further changes in the downstream pressure. The downstream pressure has the same effect on medium velocity, as shown in Figure 2. This circumstance arises because of the choke occurring above pressure (Sokolowski & Kozlowski, 2012).

2.1 Single-phase critical flow

The following equations can be used to produce the formula for single-phase critical mass flow rate.

$$h_0 = \frac{U^2}{2} + h \quad (2)$$

where, h_0 is stagnation enthalpy [kJ/kg]

h is downstream enthalpy [kJ/kg]

$$h = \frac{k}{k-1} \cdot R \cdot T = \frac{k}{k-1} \cdot \frac{p}{\rho} \quad (3)$$

where, k is Poisson's ratio [-]

R is gas constant [$\frac{J}{mol \cdot K}$]

T is temperature [K]

p is pressure [bar]

ρ is density [$\frac{kg}{m^3}$]

Assuming isentropic transition, gas enthalpy:

$$\frac{k}{k-1} \cdot R \cdot T \cdot \frac{p}{\rho} = \frac{a^2}{k-1} \quad (4)$$

Assuming that:

$$a = \sqrt{k \cdot \frac{\partial p}{\partial \rho}} = \sqrt{k \cdot \frac{p}{\rho}} = \sqrt{k \cdot R \cdot T} \quad (5)$$

The state of upstream vessel or stagnation conditions are indicated by the symbol "0" in Eqs (2). When Eqs. (2), (3), (4) and (5) are combined, and the assumptions that the stagnation velocity is minimal and the Mach number is 1, the following result is obtained:

$$a_c = a_0 \cdot \sqrt{\frac{2}{k-1}} \quad (6)$$

Critical circumstances are indicated by the notation "c." If an isentropic process is assumed:

$$\frac{p^{k-1}}{T} = const \quad (7)$$

$$\frac{T}{\rho^{k-1}} = const \quad (8)$$

And using ideal gas relations:

$$\frac{p_c}{p_0} = \left(\frac{2}{k+1}\right)^{\frac{k}{k-1}} \quad (9)$$

$$\frac{\rho_c}{\rho_0} = \left(\frac{2}{k+1}\right)^{\frac{1}{k-1}} \quad (10)$$

The following will be the critical mass flow rate:

$$m_c = \rho_c \cdot U_c \cdot A_c = A_c \cdot \frac{p_0}{\sqrt{T_0}} \cdot \sqrt{\frac{k}{R}} \cdot \sqrt{\left(\frac{2}{k+1}\right)^{\frac{k+1}{k-1}}} \quad (11)$$

where, m is mass flow rate [kg/s]

A is nozzle area [m^2]

It is easy to declare whether the single-phase flow has reached critical condition. With a two-phase flow, reaching the critical condition is more complex. The main cause of the conditions includes that there are two existent phases, which implies that there are two different sound speeds for liquid and vapour. This makes it impossible to estimate the TPCF individually. The computations are difficult and time-consuming due to the intricate nature of TPCF, such as the several flow regimes displayed. Some modelling approximations must be used to solve the challenges (Sokolowski & Kozlowski, 2012).

2.2 Two-phase critical flow

The critical flow for two-phase choking depends on the rate of vapour formation at the choke point. During the migration of fluid particles in proximity to the rupture point, the rate at which vapor forms will affect how compressible the mixture is. In the context of two-phase flow, there exists a significant variation in the density of the mixture as the pressure changes, which becomes even more pronounced compared to the gas phase. The rate of change in density with pressure is an inverse function of sonic velocity. Compared to single-phase gas flow, in two-phase flow, the sonic velocity is decreased. (Deych & Filipov, 1969). Other research indicated similar behaviour (Kieffer, 1977). For hot water at around 300 °C, the

speed of sound is about 900 m/s. For saturated steam at 300 °C, the speed of sound is 480 m/s. For bubbly flow at void fractions < 0.2, the speed of sound is in the order of 20 m/s. The generation of vapor will be influenced by the liquid superheat or the extent of nonequilibrium, flow pattern, interfacial area, and interfacial momentum transfer or slip. Figure 3 displays the observed relationship between the ratio of two-phase sonic velocity to vapor sonic velocity and the quality of the mixture.

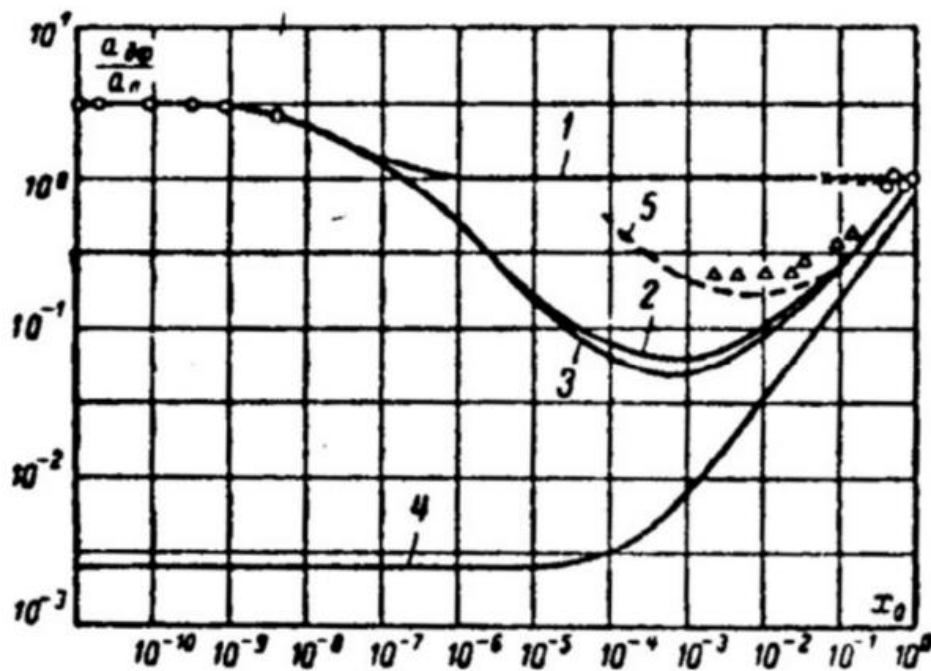


Figure 3: Ratio of two-phase sound velocity to vapor sound velocity as a function quality (D'Auria, 2017).

The production of vapor causes a rise in mixture velocity. In contrast to single-phase flow, the choke point in the case of converging-diverging nozzles may be in the diverging portion, according to Kestin (1991) and Rohatgi & Reshotko (1975). The flow can still be accelerated while compensating for area growth through vapor formation. However, there are no essential flow experiments that assess the local characteristics of two-phase flow (D'Auria, 2017).

The homogeneous equilibrium model (HEM), in which both phases move at the same speed and temperature, represents the ideal simplified state. The formula yields the lowest sonic or choking velocity and is comparable to single-phase gas flow. However, lengthy pipes with ample time for two phases to approach equilibrium conditions may contain this sort of situation (D'Auria, 2017). The lowest sound velocity is predicted by the HEM formulation.

$$G_{c,HEM}^2 = \left[(1 - x_c) \cdot \left(\frac{\partial \frac{1}{\rho_l}}{\partial p} \right)_s + x_c \cdot \left(\frac{\partial \frac{1}{\rho_g}}{\partial p} \right)_s + \left(\frac{1}{\rho_g} - \frac{1}{\rho_l} \right) \cdot \left(\frac{\partial x_c}{\partial p} \right) \right]^{-1} \quad (12)$$

where, G is mass flux $\left[\frac{kg}{m^2 \cdot s} \right]$

x is steam quality [-]

c is subscript means critical

l is subscript means liquid

s is subscript means constant entropy

g is subscript means vapor

Two mechanistic techniques which are used to study the homogeneous thermal nonequilibrium phenomena. A mixture of nucleation and bubble development was employed in one instance, while in another, the pressure at the critical point was calculated from tests. The behaviour of critical flows is determined by the conditions present at the point of rupture (D'Auria, 2017). Due to the finite pace of bubble development and nucleation, which causes the fluid pressure to undershoot the vapour pressure, it has been found that there is a delay in vapour formation during the depressurization of subcooled liquid at the rupture (Alamgir & Lienhard, 1981; Jones, 1980). According to TRACE documentation, the following pressure is the critical pressure at which vaporization will start:

$$P_l = P_{sat} - \text{Max} \left[0, 0.258 \cdot \frac{\sigma^{1.5} \cdot \left(\frac{T_l}{T_c} \right)^{13.76} \cdot \sqrt{1 + 13.25 \cdot \left(-\frac{1}{1.01325 \cdot 10^{11}} \cdot \frac{DP}{Dt} \right)^{0.8}}}{(k \cdot T_c)^{0.5} \cdot \left(1 - \frac{\rho_g}{\rho_l} \right)} - 27 \cdot (0.072)^2 \cdot \left(\frac{A_t}{A_{up}} \right)^2 \cdot \frac{\rho_l \cdot u_l^2}{2} \right] \quad (13)$$

$$u_t = \max \left[a_{HEM}, \left(u_{up}^2 + \frac{2 \cdot (p_{up} - p_l)}{\rho_l} \right)^{0.5} \right] \quad (14)$$

where, σ is surface tension [N/m]

T is stress tensor [Pa]

k is turbulent kinetic energy [m^2/s^2]

u is velocity [m/s]

t is time [s]

P is space time averaged mixture pressure [Pa]

t is subscript means throat

up is subscript means upstream

As can be seen from the expression, both surface tension and the pace at which the fluid particle's pressure changes as it goes from upstream to the throat have an impact. In situations where the pressure is below the saturation pressure, the flow is approximated using the Bernoulli equation. (D'Auria, 2017).

Few research for example, Rohatgi & Reshotko (1975) and Richter (1983) have used nucleation and bubble growth models to calculate vapor production and its impact on critical flows. Although these studies offered a foundation for modelling. They also call for a free parameter—the nucleation site density—which cannot be observed. It could differ by several orders of magnitude. Friction loss at the wall was employed in these investigations. The Fanno equations are used to determine the critical flow in the situation of gas flow with wall friction. The explanation for the decline in critical flow for gas flow is a drop in both critical flow and stagnation pressure. There are correlations that relate to the relaxation of one or more equilibrium criteria, such as non-homogenous or homogeneous nonequilibrium models (D'Auria, 2017). The most popular connections are those by Moody, Henry and Fauske, and the HEM model, which was previously discussed (Moody, 1966; Henry & Fauske, 1971). Moody loosened the equal velocity requirement while maintaining thermal equilibrium (Moody, 1965).

Here, his correlation is provided.

$$x = \frac{s_0 - s_l}{s_g - s_l} \quad (15)$$

where, s is entropy [J/kgK]

$$G_c^2 = \frac{2 \cdot [h_0 - h_l - x \cdot (h_g - h_l)]}{\left(\frac{u_g}{u_l \cdot \rho_l} \cdot (1 - x) + x \cdot \frac{1}{\rho_l}\right)^2 \cdot \left(x + (1 - x) \cdot \left(\frac{u_l}{u_g}\right)^2\right)} \quad (16)$$

Moody's slip ratio assumption.

$$S_r = \frac{u_g}{u_l} = \sqrt[3]{\frac{\rho_l}{\rho_g}} \quad (17)$$

Fauske proposed a quite different slip correlation (Fauske, 1962).

$$S_r = \frac{u_g}{u_l} = \sqrt[2]{\frac{\rho_l}{\rho_g}} \quad (18)$$

For local settings, Henry et al., provided the other often cited correlation. By lowering the quality at departure from equilibrium value, they lowered the thermal equilibrium requirement (Henry et al., 1970).

$$x = N \cdot S_r \cdot x_e \quad (19)$$

where e is subscript, refers to equilibrium.

The slide would allegedly be close to 1.0 at the choke site. For low-quality and lengthy pipes, the critical mass flux expression was empirically determined and is given as

$$N = 20 \cdot x_{eq} \text{ for } 0 < x_{eq} < 0.05 \quad (20)$$

$$N = 1 \text{ for } x_{eq} > 0.05 \quad (21)$$

$$N = \frac{G_{cr,HEM}}{\sqrt{N_{exit}}} \quad (22)$$

Additionally, Henry created correlations that included pipe length (Henry,1970). The rating for the exit quality was.

$$x_{exit} = x_{LT} \cdot \left(1 - \exp \left(-B \cdot \left(\frac{L}{D} - 12 \right) \right) \right) \quad (23)$$

where, L is length [m]
 D is diameter [m]
 B is decay constant
 LT is subscript, refers to a long tube's quality

$$x_{LT} = N \cdot x_{eq} \quad (24)$$

where eq is subscript, refers equilibrium

Henry made the assumptions that the vapor phase would expand isothermally, and the liquid would be incompressible (Henry, 1970).

$$G_{cr}^2 = \frac{1}{\left[\frac{x}{p \cdot \rho_g} - \left(\frac{1}{\rho_g} - \frac{1}{\rho_l} \right) \cdot N \cdot \frac{dx_{eq}}{dp} \right]_{exit}} \quad (25)$$

The decay constant B was suggested to be 0.0523 which was estimated by fitting the data.

The most common two-phase critical flow models were reviewed and discussed the two-phase critical flow phenomena. In the next section, part of the two-phase critical flow models is examined in more detail, as well as how they are formed.

2.3 Models of two-phase critical flow based on the Separated Flow Models

The primary distinction between the Separated Flow Model (SFM) and the simpler Homogeneous Flow Model (HEM) discussed in the following section lies in the SFM's capability to depict the two phases individually with their distinct characteristics and velocities. (Kim & Mudawar, 2015).

The fundamental separated flow model, at its core, known as the "Slip Flow Model" is based on one-dimensional flow taking into account the constant velocities within each phase while permitting variations in phase velocities. Multiple alternative relationships have been proposed to describe the critical flow behaviour in two-phase systems that have been derived using this model, as will be explained below (Kim & Mudawar, 2015).

The steady slip flow model makes the following fundamental assumptions: The liquid and vapor phases are kept apart and take up distinct areas in the flow area; The velocity profile is consistent throughout each phase; The interface between liquid and vapor is smooth; The cross-sectional area of the channel experiences a constant pressure ($P_g = P_f = P$); Based on the local saturation pressure, each phase's thermophysical characteristics are determined; Along the channel, thermodynamic equilibrium is preserved, i.e., $x = x_e$ in the two-phase area ($0 \leq x_e \leq 1$) (Kim & Mudawar, 2015). Based on the Slip Flow Model, Figure 4 illustrates the momentum and force components for two-phase flow in a channel.

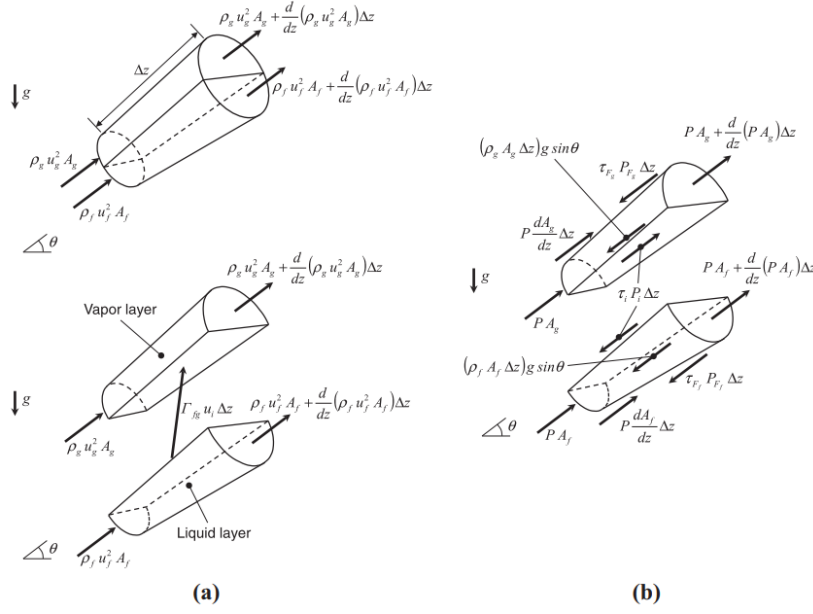


Figure 4: (a) Momentum elements for a two-phase combined flow and for different layers. (b) Components of force for each layer.

In a channel differential control volume of length Δz , momentum conservation for the vapor and liquid layers is provided, respectively, as

$$\begin{aligned} \frac{d}{dz}(\rho_g \cdot u_g^2 \cdot A_g) - \Gamma_{fg} \cdot u_i \\ = \alpha \cdot A \cdot \frac{dP}{dz} - \tau_{Fg} \cdot P_{Fg} - \tau_i \cdot P_i - \rho_g \cdot g \cdot \alpha \cdot A \cdot \sin\theta \end{aligned} \quad (26)$$

also

$$\begin{aligned} \frac{d}{dz}(\rho_f \cdot u_f^2 \cdot A_f) + \Gamma_{fg} \cdot u_i \\ = -(\alpha - 1) \cdot A \cdot \frac{dP}{dz} - \tau_{Ff} \cdot P_{Ff} + \tau_i \cdot P_i - \rho_f \cdot g \cdot (\alpha - 1) \cdot A \\ \cdot \sin\theta \end{aligned} \quad (27)$$

where, Γ_{fg} the rate at which mass is transferred as a result of evaporation at the vapor-liquid interface [kg/m^3s].

u_i interfacial axial velocity [m/s].

τ_{Fg} shear stress between the vapor layer and the wall [Pa].

τ_{Ff} shear stress between the liquid layer and the wall[Pa].

τ_i interfacial shear stress[Pa].

P_{Fg} portion of channel's perimeter covered with vapor.

P_{Ff} portion of channel's perimeter covered with liquid.

P_i interfacial perimeter.

P pressure [Pa].

z stream-wise coordinate.

α void fraction.

The subscript f refers to the liquid flow. The momentum components along the axis of the vapor and liquid layers, are reduced to the following when the formulas for flow quality, x and void fraction, α are included.

$$\rho_g \cdot u_g^2 \cdot A_g = \frac{x^2 \cdot G^2 \cdot A}{\rho_g \cdot \alpha} \quad (28)$$

also

$$\rho_f \cdot u_f^2 \cdot A_f = \frac{(1-x)^2 \cdot G^2 \cdot A}{\rho_f \cdot (1-\alpha)} \quad (29)$$

Using Eq. (28) into Eq. (26), and Eq. (29) into Eq. (27), and combining the resultant relations produces.

$$G^2 \cdot \frac{d}{dz} = \left[\frac{x^2 \cdot A}{\rho_g \cdot \alpha} - \frac{(1-x)^2 \cdot A}{\rho_f \cdot (1-\alpha)} \right] =$$

$$\alpha \cdot A \cdot \frac{dP}{dz} - (\tau_{Fg} \cdot P_{Fg} + \tau_{Ff} \cdot P_{Ff}) - [\rho_g \cdot \alpha + \rho_f \cdot (\alpha - 1)] \cdot A \cdot \sin\theta \quad (30)$$

$$\cdot g$$

The simplified version of Eq. (30) for a constant flow region is.

$$G^2 \cdot \frac{d}{dz} \left(\frac{1}{\rho'} \right) = - \frac{dP}{dz} - \frac{\tau_F \cdot P_F}{A} - \bar{\rho} \cdot g \cdot \sin\theta \quad (31)$$

where, ρ' momentum density [kg/m^3]

$\bar{\rho}$ mixture density [kg/m^3]

$$\tau_F \cdot P_F = \tau_{Fg} \cdot P_{Fg} + \tau_{Ff} \cdot P_{Ff} \quad (32)$$

$$\left(\frac{1}{\rho'} \right) = \frac{x^2}{\rho_g \cdot \alpha} - \frac{(1-x)^2}{\rho_f \cdot (1-\alpha)} \quad (33)$$

$$\bar{\rho} = [\rho_g \cdot \alpha + \rho_f \cdot (\alpha - 1)] \quad (34)$$

Eq. (30)'s convective term may be represented as

$$\frac{d}{dz} \left(\frac{1}{\rho'} \right) = \left[\frac{d}{dP} \left(\frac{1}{\rho'} \right) \right] \cdot \frac{dP}{dz} \quad (35)$$

Eq. (35) is substituted into Eq. (31) to produce.

$$- \frac{dP}{dz} = \frac{\frac{\tau_F \cdot P_F}{A} + \bar{\rho} \cdot g \cdot \sin\theta}{1 + G^2 \cdot \left[\frac{d}{dP} \cdot \left(\frac{1}{\rho'} \right) \right]} \quad (36)$$

Setting the denominator of Eq. (36) to zero results in the maximum pressure gradient by according to Fauske's theory, the pressure gradient exhibits a finite maximum value at the choke point, which results in the following equation for critical mass flux.

$$G_c = \left[- \frac{d}{dP} \cdot \left(\frac{1}{\rho'} \right) \right]^{-\frac{1}{2}} = \left\{ - \frac{d}{dP} \cdot \left[\frac{v_g \cdot x^2}{\alpha} + \frac{v_f \cdot (1-x)^2}{(1-\alpha)} \right] \right\}^{-\frac{1}{2}} \quad (37)$$

When terms in Eq. (37) are differentiated, the critical mass flux is.

(SFM Baroczy or SFM Wallis, depending on void fraction):

$$G_c = \left\{ - \left[\frac{x^2}{\alpha} \cdot \frac{dv_g}{dP} + \frac{(1-x)^2}{(1-\alpha)} \cdot \frac{dv_f}{dP} + \left(\frac{2 \cdot v_g \cdot x}{\alpha} - \frac{2 \cdot v_f \cdot (1-x)}{(1-\alpha)} \right) \cdot \frac{dx}{dP} - \left(\frac{v_g \cdot x^2}{\alpha^2} - \frac{v_f \cdot (1-x)^2}{(1-\alpha)^2} \right) \cdot \frac{d\alpha}{dP} \right] \right\}^{-\frac{1}{2}} \quad (38)$$

where, v specific volume [m^3/kg]

It is straightforward to calculate the derivatives in Eq. (38) using tables containing information about saturated properties. The derivative associated with interfacial mass transfer between the phases can be determined using either the isentropic or isenthalpic flow hypotheses, or based on thermodynamic relations, as will be covered later. The Baroczy void fraction relation may be used to estimate the derivative of void fraction concerning pressure, (Kim & Mudawar, 2015).

$$\alpha = \left[1 + \left(\frac{1-x}{x} \right)^{0.74} \cdot \left(\frac{v_f}{v_g} \right)^{0.65} \cdot \left(\frac{\mu_f}{\mu_g} \right)^{0.13} \right]^{-1} \quad (39)$$

From α regarding pressure, Eq. (39) will be derived. Calculations using saturation property may be used to get the derivatives $d\mu_g/dP$ and $d\mu_f/dP$. The Lockhart-Martinelli parameter can also be used to correlate the void fraction relation. Wallis came up with the relationship (Kim&Mudawar, 2015).

$$\alpha = (1 + X_{tt}^{0.8})^{-0.378} \quad (40)$$

By using a Lockhart-Martinelli parameter that is based on the combination of turbulent liquid and turbulent vapor fluxes to match void fraction data,

$$X_{tt} = \left(\frac{1}{x} - 1 \right)^{0.9} \cdot \left(\frac{v_f}{v_g} \right)^{0.5} \cdot \left(\frac{\mu_f}{\mu_g} \right)^{0.1} \quad (41)$$

where, μ dynamic viscosity [$Pa \cdot s$]

The slip ratio, S_r , which is referred to as the ratio of vapor velocity to liquid velocity, $S_r = u_g/u_f$, may be used to relate the void percentage in Eq. (37). According to the flow quality definition,

$$x = \frac{\rho_g \cdot u_g \cdot A_g}{\rho_g \cdot u_g \cdot A_g + \rho_f \cdot u_f \cdot A_f} = \frac{1}{1 + \frac{\rho_f}{\rho_g} \cdot \frac{1}{S_r} \cdot \left(\frac{1-\alpha}{\alpha}\right)} \quad (42)$$

Produces the relationship shown below for the relationship between void fraction and slip ratio, specific volume ratio, and flow quality.

$$\alpha = \frac{1}{1 + S_r \cdot \frac{v_f}{v_g} \cdot \left(\frac{1-x}{x}\right)} \quad (43)$$

Eq. (43) is substituted into Eq. (33) to produce.

$$\frac{1}{\rho'} = v_g \cdot x^2 + v_f \cdot S_r \cdot x \cdot (1-x) + \frac{v_g \cdot (1-x) \cdot x}{S_r} + v_f \cdot (1-x)^2 \quad (44)$$

Differentiating Eq. (44) in terms of pressure. The critical mass flux is then calculated using Eq. (37).

(SFM Moody):

$$G_c = \left\{ - \left[\left(x^2 + \frac{x \cdot (1-x)}{S_r} \right) \cdot \frac{dv_g}{dP} + \left((1-x)^2 + S_r \cdot x \cdot (1-x) \right) \cdot \frac{dv_f}{dP} \right. \right. \\ \left. \left. + \left(2 \cdot v_g \cdot x + \frac{v_g \cdot (1-2 \cdot x)}{S_r} + v_f \cdot S_r \cdot (1-2 \cdot x) - 2 \cdot v_f \right. \right. \right. \\ \left. \left. \cdot (1-x) \right) \cdot \frac{dx}{dP} + x \cdot (1-x) \cdot \left(v_f - \frac{v_g}{S_r^2} \right) \cdot \frac{dS_r}{dP} \right\}^{-\frac{1}{2}} \quad (45)$$

According to Fauske and Moody the critical flow rate can be determined using theoretical models of annular two-phase flow. The slip ratio in both models was depicted as a function that correlated with the specific volume ratio. Fauske got $S_r = (v_g/v_f)^{1/2}$ by reducing the momentum density provided by Eq. (44) in the critical cross section, i.e., by setting.

$$\frac{d\left(\frac{1}{\rho'}\right)}{dS_r} = x \cdot (1-x) \cdot \left(v_f \cdot \frac{v_g}{S_r^2}\right) = 0 \quad (46)$$

Moody, on the other hand, produced $S_r = (v_g/v_f)^{1/3}$ by optimizing the two-phase flow rate, as will be detailed later. Moody's slip ratio is the same as Zivi's, who reduced kinetic energy flux in the crucial cross-section (Kim&Mudawar, 2015).

2.3.1 Critical mass flux according to Fauske's relation

Fauske's slip ratio relation, S_r , substituted into Eq. (45) yields.

(SFM Fauske):

$$\begin{aligned} G_c = & \left\{ - \left[\left(x^2 + \frac{x \cdot (1-x)}{S_r} \right) \cdot \frac{dv_g}{dP} + \left((1-x)^2 + S_r \cdot x \cdot (1-x) \right) \cdot \frac{dv_f}{dP} \right. \right. \\ & + \left(2 \cdot v_g \cdot x + \frac{v_g \cdot (1-2 \cdot x)}{S_r} + v_f \cdot S_r \cdot (1-2 \cdot x) - 2 \cdot v_f \right. \\ & \left. \left. \cdot (1-x) \right) \cdot \frac{dx}{dP} \right] \Bigg\}^{-\frac{1}{2}} \quad (47) \end{aligned}$$

Given that $dx/dP=0$ for two-phase flows without mass transfer (such as air-water flow), and $dv_f/dP \ll dv_g/dP$ for very low pressures (up to 2.66 MPa for steam-water), Eq. (47) may be simplified for low pressure adiabatic flow as.

(SFM Fauske simple):

$$G_c = \left\{ - \left(x^2 + \frac{x \cdot (1-x)}{S_r} \right) \cdot \frac{dv_g}{dP} \right\}^{-\frac{1}{2}} \quad (48)$$

2.3.2 Critical mass flux according to Moody's relation

Moody created a simple Slip Flow Model based on the presumption of two-phase annular flow that is isentropic via a nozzle, where the velocities of the liquid and vapor are given, respectively, as

$$u_f = \frac{G \cdot (1-x)}{\rho_f \cdot (1-\alpha)} \quad (49)$$

$$u_g = \frac{G \cdot x}{\rho_g \cdot \alpha} \quad (50)$$

The equation that describes the energy balance in a system with adiabatic and frictionless flow, or isentropic flow, is defined by the condition that the stagnation entropy remains constant.

$$s_0 = s_f + x \cdot s_{fg} \quad (51)$$

$$h_0 = x \cdot \left(h_g + \frac{u_g^2}{2} \right) + (1-x) \cdot \left(h_f + \frac{u_f^2}{2} \right) \quad (52)$$

The subscript fg refers to the distinguishing characteristics between different instances of vapor in a saturated state and liquid in its saturated state. The following formula for mass flux is produced by integrating the connections of phase velocities, Eqs. (49) and (50), stagnation characteristics, Eqs. (51) and (52), and void fraction, Eq. (43).

$$G = \left\{ \frac{2 \cdot \left[h_0 - h_f - \frac{h_{fg}}{s_{fg}} \cdot (s_0 - s_f) \right]}{\left[\frac{S_r \cdot (s_g - s_0) \cdot v_f}{s_{fg}} + \frac{(s_0 - s_f) \cdot v_f}{s_{fg}} \right]^2 \cdot \left[\frac{s_0 - s_f}{s_{fg}} + \frac{s_g - s_0}{S_r^2 \cdot s_{fg}} \right]} \right\}^{\frac{1}{2}} \quad (53)$$

The following relationships must be met by this equation at the maximum flow condition since Eq. (53) is a function of pressure and slip ratio.

$$\left. \frac{\partial G}{\partial S_r} \right|_P = 0 \quad (54)$$

$$\left. \frac{\partial G}{\partial P} \right|_{S_r} = 0 \quad (55)$$

Eq. (54) is used to get the Moody's equation governing the slip ratio during the maximum flow condition. The critical mass flux may then be determined iteratively using Eqs. (53) and (55). Using Eqs. (53)-(55), Moody derived the following relationship between critical mass flux and local static characteristics.

(SFM Moody):

$$G_c = \left[-\frac{2 \cdot (v_f + x \cdot v_{fg})}{a \cdot (a \cdot d + 2 \cdot b \cdot e)} \right]^{\frac{1}{2}} \quad (56)$$

$$a = S_r \cdot v_f + x \cdot (v_g - S_r \cdot v_f) \quad (57)$$

$$b = \frac{1}{S_r^2} + x \cdot \left(1 - \frac{1}{S_r^2} \right) \quad (58)$$

$$d = \left[\frac{1}{S_r^2 \cdot s_{fg}} \frac{ds_g}{dP} - \frac{1}{s_{fg}} \frac{ds_f}{dP} - \frac{1}{S_r^4 \cdot s_{fg}} \frac{d}{dP} (s_{fg} \cdot S_r^2) \right] \quad (59)$$

$$\begin{aligned}
& +x \cdot \left[\frac{1}{S_r^4 \cdot s_{fg}} \frac{d}{dP} (S_r^2 \cdot s_{fg}) - \frac{1}{s_{fg}} \frac{ds_{fg}}{dP} \right] \\
e & = \left[s_{fg} \frac{d}{dP} \left(\frac{S_r \cdot v_f}{s_{fg}} \right) + \frac{S_r \cdot v_f}{s_{fg}} \frac{ds_g}{dP} - \frac{v_g}{s_{fg}} \frac{ds_f}{dP} \right] \\
& +x \cdot \left[s_{fg} \frac{d}{dP} \left(\frac{v_g}{s_{fg}} \right) - s_{fg} \frac{d}{dP} \left(\frac{S_r \cdot v_f}{s_{fg}} \right) \right]
\end{aligned} \tag{60}$$

For the slip ration will be used Moody's slip ration that was mentioned earlier.

2.3.3 Models of two-phase critical flow based on the Homogeneous Equilibrium Model (HEM)

Within the Homogeneous Equilibrium Model (HEM), a pseudo fluidity is assigned to a two-phase mixture, where uniform properties are maintained throughout the flow region. The model further postulates the uniformity of velocity and phase velocities across the flow region. Since $S_r = 1$, Eq. (43) produces the void fraction relationship (Kim&Mudawar, 2015).

$$\alpha = \frac{1}{1 + \frac{v_f}{v_g} \cdot \left(\frac{1-x}{x} \right)} \tag{61}$$

Inputting Eq. (61) into Eq. (33) results in

$$\frac{1}{\rho'} = x \cdot v_g + v_f \cdot (1-x) \tag{62}$$

The following formula for the HEM critical mass flow is acquired through the process of differentiation Eq. (62) relative to the pressure variable and putting it into Eq. (37).

$$G_c = \left\{ - \left[x \frac{dv_g}{dP} + (1-x) \frac{dv_f}{dP} + (v_g - v_f) \frac{dx}{dP} \right] \right\}^{-\frac{1}{2}} \quad (63)$$

We shall now examine more closely the following models such as non-flashing two-phase flow, isenthalpic two-phase flow, isentropic two-phase flow, and isentropic two-phase flow using thermodynamic relations.

Eq. (63) the expression for the critical mass flux in the homogeneous frozen (non-flashing) model can be simplified as follows. eq. (64) where the interfacial mass transfer can be considered insignificant (i.e., $dx/dP = 0$). Eq. (64) was developed by Wallis for homogeneous flow with negligible flashing. It is possible to determine the rate of change of quality with respect to pressure, dx/dP , by applying thermodynamic relations, isentropic or isenthalpic assumptions, or both. (Kim&Mudawar, 2015, 504).

(Homogenous frozen model (HFM)):

$$G_c = \left\{ - \left[x \frac{dv_g}{dP} + (1+x) \frac{dv_f}{dP} \right] \right\}^{-\frac{1}{2}} \quad (64)$$

Enthalpy is constant in an isenthalpic process, and when paired with equation (63), the critical mass flux is given by the following relation.

(HEM isenthalpic):

$$G_c = \left\{ - \left[x \cdot \frac{dv_g}{dP} + (1+x) \cdot \frac{dv_f}{dP} - \frac{v_{fg}}{h_{fg}} \cdot \left(\frac{dh_f}{dP} + x \cdot \frac{dh_{fg}}{dP} \right) \right] \right\}^{-\frac{1}{2}} \quad (65)$$

Entropy remains constant during an isentropic process, and when paired with equation (63), the critical mass flux is given by the following relation

(HEM isentropic):

$$G_c = \left\{ - \left[x \cdot \frac{dv_g}{dP} + (1+x) \cdot \frac{dv_f}{dP} - \frac{v_{fg}}{s_{fg}} \cdot \left(\frac{ds_f}{dP} + x \cdot \frac{ds_{fg}}{dP} \right) \right] \right\}^{-\frac{1}{2}} \quad (66)$$

Another isentropic model that uses thermodynamic relationships that are employed in the determination of the critical mass flux within an isentropic two-phase flow. The thermodynamic relation for an isentropic process is reduced to.

$$dh - v dP = d(h_f + x \cdot h_{fg}) - (v_f + x \cdot v_{fg}) dP = 0 \quad (67)$$

The alterations in enthalpy for vapor and liquid phases can be denoted by the subsequent expressions when taking into account enthalpy as a function of temperature and pressure.

$$dh_g = c_{p,g} \cdot dT \quad (68)$$

$$dh_f = c_{p,f} \cdot dT + v_f \cdot (1 - \beta \cdot T) \cdot dP \quad (69)$$

$$\beta = \frac{1}{v_f} \cdot \left. \frac{\partial v_f}{\partial T} \right|_P \quad (70)$$

The β is the volumetric thermal expansion coefficient. Because the pressure change term in Eq. (68) is considerably smaller in comparison to the term representing the temperature change, it is ignored. Using the Clapeyron equation.

$$\frac{dT}{dP} = \frac{T \cdot v_{fg}}{h_{fg}} \quad (71)$$

The following formula for the critical mass flux is produced by combining Eqs. (67)-(71) and (63).

(HEM isentropic using thermodynamic relations):

$$G_c = \left\{ - \left[x \cdot \frac{dv_g}{dP} + (1-x) \cdot \frac{dv_f}{dP} + (v_g - v_f) \right. \right. \\ \cdot \left(\frac{v_f + x \cdot v_{fg}}{h_{fg}} - x \cdot c_{p,g} \cdot \frac{T \cdot v_{fg}}{h_{fg}^2} - \frac{(1-x)}{h_{fg}} \right. \\ \left. \left. \cdot \left(c_{p,f} \cdot \frac{T \cdot v_{fg}}{h_{fg}} + v_f \cdot (1 - \beta \cdot T) \right) \right) \right] \right\}^{-\frac{1}{2}} \quad (72)$$

2.4 Conclusions of two-phase critical flow models

Several publications delve into the extensive array of models and tests that are available for studying critical flows (Saha, 1978; Elias&Lellouche, 1994; Levy, 1999; Sokolowski et al., 2012; Brittain et al., 1982; Miller, 2010; OECD/NEA/CSNI, 1980) (D'Auria, 2017, 601).

Elias and Lellouche, in their publication of 1994, documented 66 experiments involving diverse lengths, diameters, and pressures. Nonetheless, out of the experiments conducted, only 42 data sets proved to be viable. In the experiments diameters of discharge nozzles/pipes ranged from 4mm to 76 mm. The lengths varied between zero to 1700 mm. A set of data from Marviken was significantly more pertinent to the reactor system. The pipe's length ranged from 166 to 1800 mm, while its diameter ranged from 200 to 500 mm. According to Elias and Lellouche's investigation, no model adequately accounted for the data. Most of the data were outside of the $\pm 10\%$ of the mean line, according to the scatter plots (D'Auria, 2017, 601). Saha has previously examined several models and came to the following conclusions (Saha, 1978):

1. In cases involving short pipelines and situations near liquid saturation or subcooled upstream conditions, the Homogeneous Equilibrium Model (HEM) tends to underestimate the critical flow rates. (Saha,1978).
2. While the equilibrium slips models proposed by Fauske, Moody, and others are effective for long tubes, they tend to underestimate the critical flow rates in short pipes. This is particularly true when the upstream state is subcooled or near saturation (Saha,1978).
3. When dealing with short pipelines, it becomes imperative to account for the impacts of thermal nonequilibrium. However, it remains uncertain whether the ramifications of thermal nonequilibrium are dependent on the length of the pipe, the pipe length-to-diameter ratio, or a combination of both factors (Saha,1978).

A systematic scaling investigation has not been conducted thus far to examine the critical flow phenomena. Dimensionless groups that encompass subcooling, flow rate, slip, wall friction, nucleation sites, break geometry, and two-dimensional effects have not been utilized for data collection, despite the identification of sub-phenomena that influence the critical mass flux. Nondimensional analyses were used by Deych and Filipov, who also identified the groups in charge of controlling flow conditions and critical flow (Deych&Filipov,1969). They used two-phase transfer terms for nondimensional fundamental equations of two-fluid balance. For comparing dimensionless numbers, they used Strouhal (transient case), Euler, Reynolds, Froude, Weber, Peclet, Prandtl, Mach, and Nusselt (at the interface) (D'Auria, 2017, 601).

3 State-of-the-art in two-phase critical flow modelling

"Separate Effects Test Matrix for Thermal Hydraulic Code Validation" was released by OECD CSNI in 1993. The best data sets for evaluation, validation, and refinement of code predictions of the many physical phenomena, including critical flow, were sought for. SET data is chosen for model creation and improvement. The validation matrix included a list of several SETs divided into three classes: pipes and valves ($L/D > 5$) and breaks ($L/D < 1$). In

this work, from the validation matrix list most suitable for the topic test facilities with a different L/D ratio are examined (OECD,1993).

Also, the FONESYS conducts experimental, theoretical, and numerical studies to understand the behaviour of two-phase critical flow and develop improved SYS-TH codes and methods for its prediction and control. Their research aims to contribute to the development of safer and more efficient energy systems. To evaluate the effectiveness of the SYS-TH codes, 92 experiments using 6 different Separate Effect Test Facilities under steady and transient settings were selected (Lanfredini&Lutsanych, 2020). Those test facilities are: Super CANON (Riegel, 1978), Edwards Pipe (Edwards&O'Brien, 1970), UCL Experiment (Attou et al., 2000), Super Moby-Dick (Sekri, 1982), Sozzi-Sutherland (Sozzi&Sutherland, 1975), Brookhaven National Laboratory (Abuaf et al., 1981).

Several key SETs are described in the following subchapters based on the validation matrix and those experiments that frequently appear in the literature while validating new models. The test facilities that will be described are:

- Super Moby Dick (Centre d'Etudes Nucléaires de Grenoble in France)
- Marviken (Marviken power plant)
- Experimental study on a two-phase critical flow with a non-condensable gas at high pressure conditions (The advanced integral reactor SMART's critical flow test facility, KAERI)
- Experimental study of the critical flashing flow through a relief line; evidence of the double-choked flow phenomena
- High-pressure water flow through narrow, sharp-edged tubes in a state of critical flow
- A metastable jet model for leaks in steam generator tube (MPA University of Stuttgart's modular fluid-structure-interaction (FSI) test facility)
- A study of subcooled choked flow in real steam generator tube cracks.

The OECD's TIETHYS database has some limited information on various SETs. the following subchapters are derived from basis of summary report by Pyy (2022) made in CRITFLO project under SAFIR2022 National Research Program.

3.1 Super Moby Dick

The Super Moby Dick Experiments, conducted at the Centre d'Etudes Nucléaires de Grenoble in France, aimed to investigate the steady-state critical flow through nozzles at medium to high pressure across different thermal-hydraulic conditions. (TRACE V5.0 ASSESSMENT MANUAL Appendix B: Separate Effects Tests). The facility is presented in Figure 5.

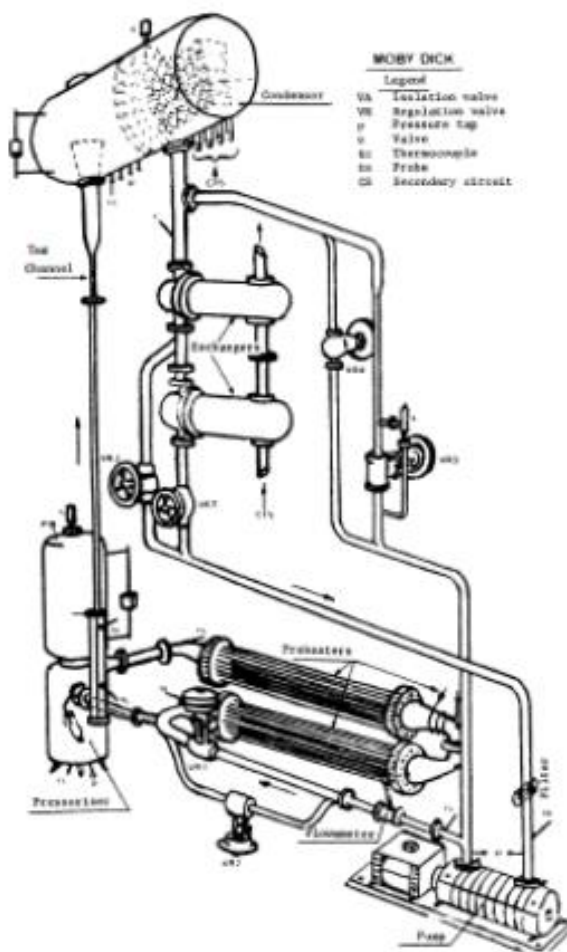


Figure 5: Super Moby Dick Experimental Facility (TRACE V5.0 ASSESSMENT MANUAL Appendix B: Separate Effects Tests)

The Super Moby Dick test facility consisted of four main components in its primary loop: a pump, a 4 MW preheater, a test section, and a condenser. Within the test section, three different geometries were utilized: a long nozzle, an abrupt expansion, and a short nozzle. The testing involved vertically injecting subcooled water through the test section and venting it to the condenser. The test section's intake conditions were kept constant to achieve critical

flow conditions, while the condenser's downstream pressure was decreased until it had no further effect on flow. At that time, choking is characterized as occurring (TRACE V5.0 ASSESSMENT MANUAL Appendix B: Separate Effects Tests). Figure 6 presents the long nozzle test section.

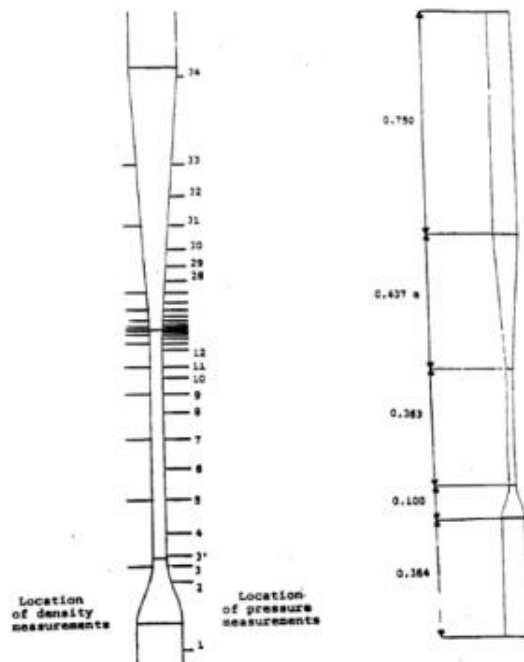


Figure 6: Super Moby Dick Long Nozzle Test Section (TRACE V5.0 ASSESSMENT MANUAL Appendix B: Separate Effects Tests)

The long nozzle test portion was made up of a 100 mm long, conical convergent nozzle with an inner diameter of 66.7 mm that was connected to a 363 mm long, 20.13 mm inner diameter pipe. A 7° conical diverging nozzle with a length of 437 mm was placed after the straight pipe portion. Both the intake and output pipes had lengths of 364 mm and 750 mm, respectively (TRACE V5.0 ASSESSMENT MANUAL Appendix B: Separate Effects Tests).

The experiments were conducted within a pressure range spanning from 4 MPa to 12 MPa. Using various subcooling levels and intake quality. In total 34 pressure transducers were installed in the long nozzle test portion. Platinum resistive probes were used to gauge the inlet's temperature. A turbine flow meter and a dynamic pressure pitot tube were used to monitor the mass flow rate. Although it wasn't used in every test, density was assessed using an X-ray densitometer from 15 window locations. (TRACE V5.0 ASSESSMENT

MANUAL Appendix B: Separate Effects Tests). An example of a two-phase critical flow measurement in the Super Moby-Dick experiment can be seen in Figure 7.

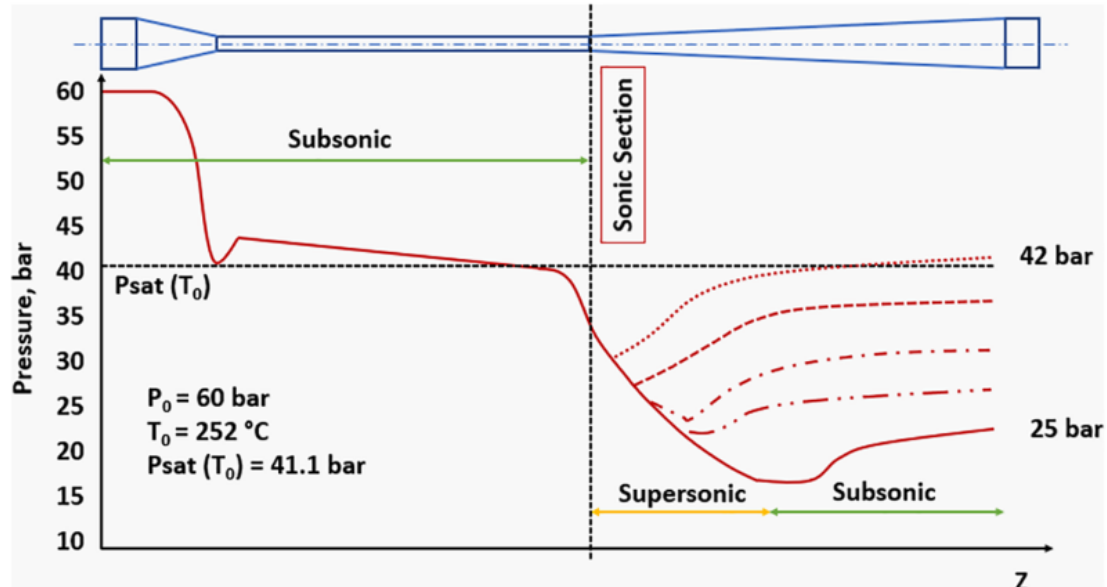


Figure 7: Example of TPCF as measured in the Super Moby-Dick experiment (M. Lanfredini et al., 2020).

The Super Moby Dick program was conducted to highlight the interphase mass and momentum transfers under a large variety of pressure conditions. The most complete, important, and trustworthy data for the high-pressure range of 4 MPa to 12 MPa comes from the Super Moby Dick two-phase critical flow experiments (Aksan et al., 1994).

3.2 Marviken

Between mid-1977 and December 1979, the Marviken power plant underwent Full Scale Critical Flow Tests (CFT). A global/multi-national project was Marviken CFT. VTT was one of the project's sponsors. 27 CFT experiments in all were carried out. For the experiments, a large-scale discharge pipe was utilized to transport water and steam-water mixtures from a full-sized reactor vessel. The flow was directed towards the test nozzles for further analysis. The test nozzles featured rounded openings and a cross section with a nominal diameter of 200, 300, or 500 mm. Their lengths ranged from 166 to 1809 mm. There were three distinct nozzle geometries used (Hall&Ericson, 1979).

Testing 1 through 12 was done using the nozzle shape shown in the Figure 8. A nozzle shape depicted in Figure 9 was used for tests 13 and 14. Testing 15–27 was done using the nozzle shape shown in Figure 10.

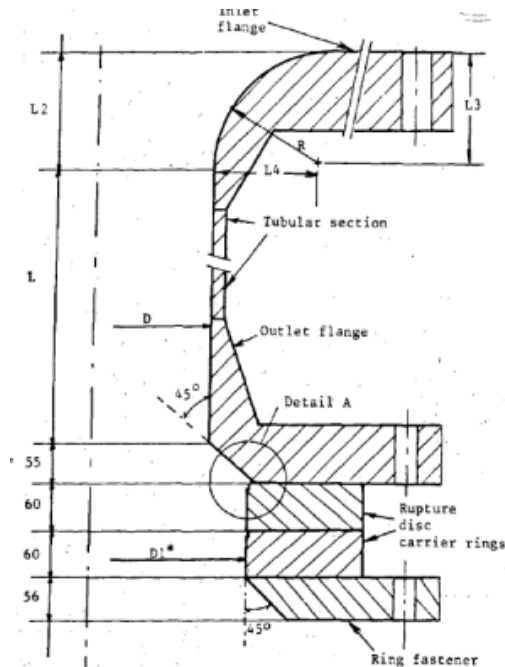


Figure 8: Nozzle used in Marviken CFT 1-12 (Sokolowski&Kozlowski, 2012)

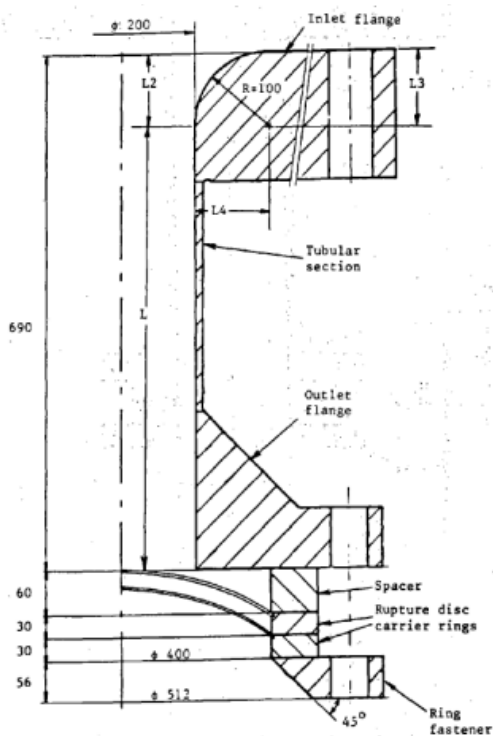


Figure 9: Nozzle geometry used in Marviken CFT 13 and 14 (Sokolowski&Kozlowski, 2012)

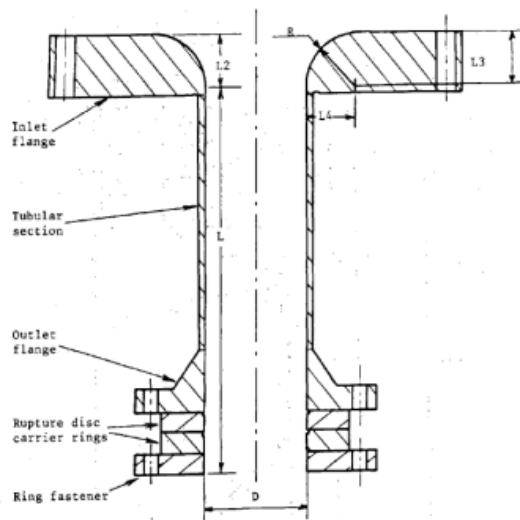


Figure 10: Nozzle geometry used in Marviken CFT 15-27 (Kozłowski&Sokolowski ,2012)

Except for one test, which used a starting pressure of 4 MPa, the tests were all done at a notional steam dome pressure of 5 MPa. Regarding the steam dome pressure, the water subcooling was varied between 50°C and 1°C. The test facility consisted of a pressure vessel with a net volume of 425 m³. The pressure vessel had a maximum design pressure of 5.75 MPa and a maximum design temperature of 272 °C. The test facility's diagram is shown in Figure 11. The discharge pipe shown in Figure 12 was coupled with the test nozzles and rupture disc assembly. The discharge pipe comprises seven components, including a connecting piece, two pipe spools, two instrumentation rings, and an isolation ball valve. It also has an axisymmetric input section. Welding the connecting piece into a 1030 mm-diameter hole drilled in the vessel's bottom allowed this assembly to be fastened to it. The input part, which is connected to the connecting piece's upstream end, permits fluid to enter the discharge pipe's 752 mm diameter smoothly from 740 mm above the vessel's bottom. From the discharge pipe entrance to the discharge pipe's terminus, the flow moves 6.3 meters (nozzle entrance) (Hall & Ericson, 1979).

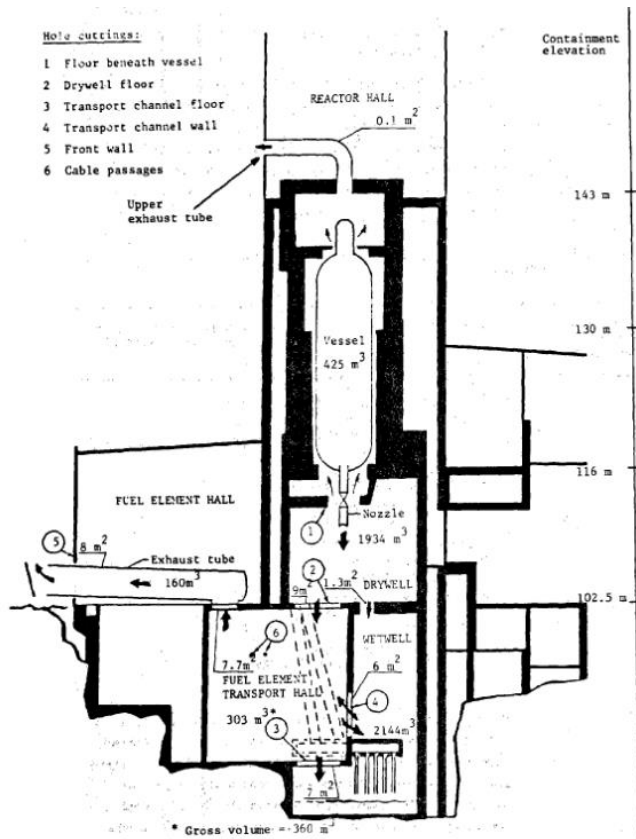


Figure 11: Test equipment installation and flow paths in the test facility building (Hall&Ericson,1979)

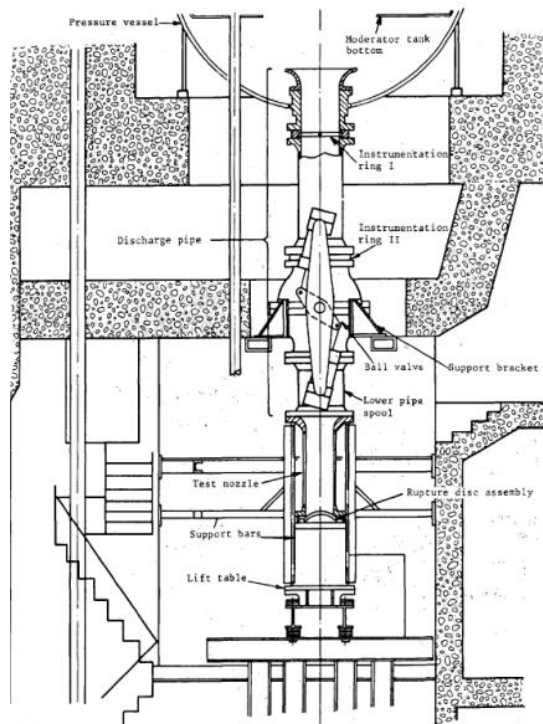


Figure 12: Discharge pipe where the different test nozzles were attached in Marviken CFT (Sokolowski et al.,2012)

The discharge steam-water mixture was released into a container via the test nozzles. Exhaust tubes linked the confinement to atmospheric conditions. The measurement methods utilized in Marviken CFT were strain gauge-type transducers with two separate measuring ranges for absolute pressure and differential pressure. For temperature readings in the tank, discharge pipe, and nozzle, chrome-alumel thermocouples were used. The thermocouples were type K and featured an insulated measurement connection. A three-beam gamma densitometer, installed before Test 9, was also used to measure density (Hall&Ericson,1979).

Mass-DP data were used to analyse the vessel mass histories. Based on a collapsed liquid level assumption and saturated steam at the steam dome, the masses were assessed. The volume average vessel temperature and the steam dome pressure were taken as the starting points for the liquid density estimation. Three distinct techniques were used to determine the nozzle mass flow rates. A steam dome expansion mechanism was employed during the first few tenths' seconds of the first discharge phase. The mass flow rates were calculated based on the densities at the nozzle entry and the volume expansion of the steam dome. The steam dome's rate of depressurization, under the assumption of an isentropic process, was used to calculate the volume expansion. By calculating the rate at which the vessel's mass changed over time, the mass inventory approach was also used to calculate the mass flow rates. The discharge pipe-based pitot static measurements were used as the third way of calculating the mass flow rate. Based on the fluid's temperature and pressure in the discharge pipe, the densities of the subcooled fluid were calculated. The three-beam gamma densitometer or DP measurements from a DP probe within the vessel near the discharge pipe inlet were both used to assess the two-phase densities. The data were measured at a frequency of 925 Hz. The precise measurement sites, data analysis techniques, and facility upgrades are provided in full (Marviken Full Scale Critical Flow Tests Summary Report, 1982).

To confine the fluid in the upstream circumstances, a configuration consisting of two rupture discs with a pressure chamber between them was used, and the tests were launched by failing the disc assembly. The tests were transitory, to obtain the dependence of critical mass flow rates on stagnation conditions using the Marviken full-scale CFT (upstream stagnation pressure, upstream stagnation enthalpy, nozzle length, nozzle diameter, and air concentration) (Marviken Full Scale Critical Flow Tests Summary Report, 1982).

MXC-17 and MXC-23 Marviken critical flow tests were utilized as validation data sets in Apros for critical flow in breaks ($L/D < 1$) and test MXC-17 for critical flow in pipes ($L/D > 5$). Throughout the code verification process, these tests are calculated with each new code version (Karppinen,2016).

3.3 Experimental study on a two-phase critical flow with a non-condensable gas at high pressure conditions.

Investigations involving experimental research on high-pressure two-phase critical flow incorporating non-condensable gas circumstances was published in 2007 by Park, H-S. et al., The advanced integral reactor SMART's critical flow test facility was developed and built at KAERI to imitate a pipe break event when most of the reactor coolant system is housed inside the reactor vessel. Nitrogen gas, steam, and water are poured into the SMART pressurizer. Three gas cylinders and the pressurizer are linked via three penetrating pipes. The prediction of the mixture is crucial at critical flow circumstances because if the connecting pipe bursts, nitrogen-steam/water mixture will be released into the reactor vessel. Figure 13 displays the test facility's schematic diagram (Park et al., 2007).

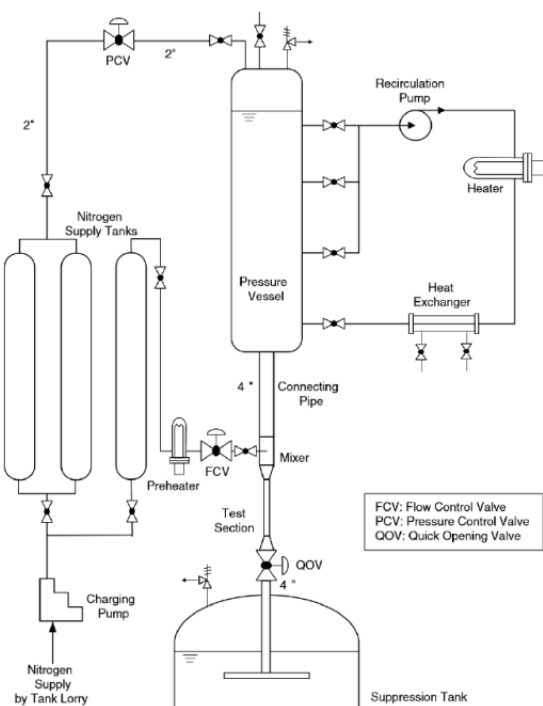


Figure 13 : KAERI Non-condensable gas two-phase critical flow test facility (Park et al., 2007)

The primary components of the setup include the pressure vessel, test section, suppression tank, and nitrogen supply tanks. The pressure vessel has a circulation loop that makes it possible to keep the temperature and pressure at the necessary stagnation levels. In a two-phase system, the reservoir pressure holds significantly greater importance, and the temperature of the coolant (reservoir) becomes interconnected with the pressure only once saturation conditions are achieved. The pressure vessel is characterized by an inner diameter of 0.57 m, a length of 5.092 m, and a total volume of 1.3 m³. A connecting pipe, measuring 2.36 m in length and featuring an inner diameter of 87.3 mm, is connected to the pressure vessel. Additionally, a flow meter is installed within the connecting pipe to measure the critical flow rate (FisherRosemount ProBar, PBR +26S). To reach the present stagnation pressure, nitrogen is delivered to the pressure vessel. Furthermore, nitrogen is injected upstream of the test area for non-condensable gas tests. The coolant that is discharged is combined with nitrogen. The mixing chamber, where the thermo-hydraulic parameters are monitored, lies above the test portion. The experiments make use of two separate test sections. Test section T2 comprises a sharp-edged stainless-steel pipe, measuring 1000 mm in length and 3.2 mm in thickness. The inner diameter of the pipe is 10.9 mm. It is equipped with 18 pressure taps and five thermocouples to measure pressure and temperature dispersion. Similar in size to T2, a single-beam gamma densitometer is utilized in the second test section T2GDM to measure the void fraction. Coolant that has been discharged is collected in a suppression tank (Park et al., 2007).

The following is a description of the experimental process: The nitrogen gas charging system uses the nitrogen gas supply tank to hold the high-pressure nitrogen gas. Water is filled into the pressure vessel until the predetermined level is reached. The water undergoes heating and circulation, facilitated by the installed heater and pump from the main circulation system, until the pressure vessel attains the desired stagnation temperature. To create a stagnation pressure, nitrogen gas is introduced into the pressure vessel. With a pressure control valve (PCV), attached to the tank that supplies nitrogen gas, the pressure is kept constant. When the experimental circumstances are met, to discharge the water from the pressure vessel, a quick-opening valve (QOV) with a minimum opening time of 1 s is activated. To simulate the flow of non-condensable gas, nitrogen gas is introduced upstream of the test section. A flow control valve (FCV) is employed to regulate the flow rate. The discharged coolant and nitrogen are then mixed together in a mixer. Once the pressure vessel reaches the desired stagnation state, the data acquisition system (DAS) is activated to

commence data recording. The experiment is over, and the DAS shuts off when the water level falls below a specified level. Various steady-state statistics are gathered, including the critical flow rate, stagnation pressure and temperature, as well as the void fraction. (Park et al., 2007)

Using two test sections and 98 runs total, various stagnation conditions were used. In 23 runs, T2 was utilized, and in 75 runs, T2GDM. Injection rates of nitrogen gas ranged from 0.0 to 0.22 kg/s. Figure 14 shows critical mass fluxes in relation to the stagnation temperatures. Figure 15 demonstrates the influence of non-condensable gas on the critical mass flow at various subcooling levels at 7 MPa (Park et al., 2007).

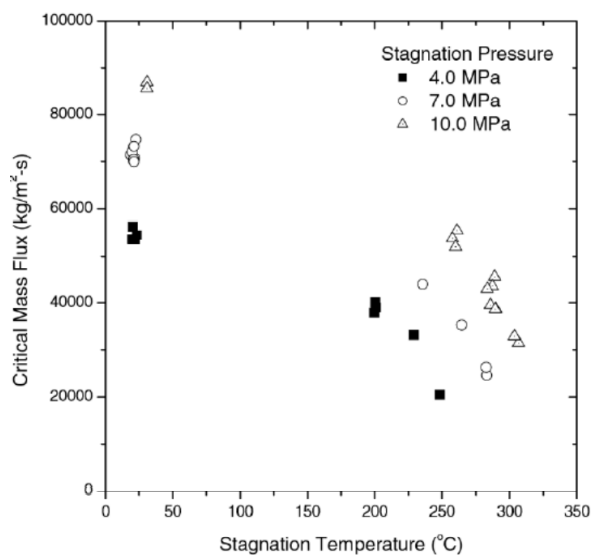


Figure 14: critical mass fluxes in relation to the stagnation temperatures (Park et al., 2007)

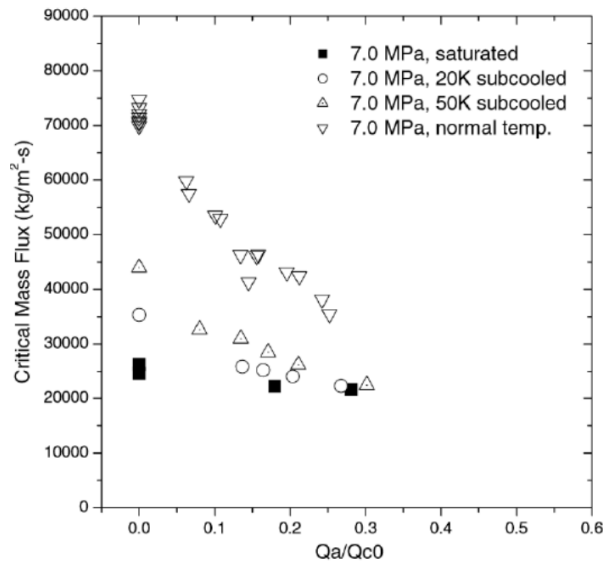


Figure 15: impact of non-condensable gas on critical mass flow at various subcooling levels (Park et al., 2007)

The critical mass flow clearly depends on the non-condensable gas portion. The impact decreases once the saturation temperature is attained. Moreover, the heat exchange within the system is significantly impacted by the subcooling level, as demonstrated in studies when non-condensable gas is not present. The publication's main results came to the following conclusion: As the stagnation pressure and inlet subcooling increased, the critical mass flux exhibited an upward trend. The percentage of non-condensable gas played a significant role in determining the critical mass flux, as it decreased rapidly with an increase in the volumetric rate of non-condensable gas. (Park et al., 2007).

3.4 Experimental study of the critical flashing flow through a relief line: evidence of the double-choked flow phenomena

Attou, A. et al., reported the experimental results of a steady-state critical steam-water flow over a horizontal relief line, which incorporated an abrupt cross-sectional area shift, in their publication in 2000. Two geometrical singularities, one with a circular aperture and the other with a rapid expansion, were tested. With increasing back pressure, the stagnation temperature ranged from 110 °C to 150 °C while the stagnation pressure remained constant at 0.6 MPa. Relief lines are built downstream of safety equipment used to safeguard pressure

containers or reactors, such as safety valves and rupture discs. Relief lines are characterized by various singularities such as sudden changes in area like expansions or contractions and abrupt changes in direction such as elbows or tee junctions. The main focus of the study was to provide new experimental insights into the steady-state flashing water flow through a discharge line featuring a single geometric singularity. (Attoul et al., 2000).

Hot, pressured water was pumped into the upstream vessel. A boiler was used to circulate and heat the water to the necessary temperature. The boiler was unplugged from the vessel during discharge. Throughout the whole blowdown experiment, the pressure in the vessel was maintained via a pneumatic control mechanism. The downstream vessel was a catch tank that was joined to the atmosphere. The test facility can be seen from Figure 16 (Attoul et al., 2000).

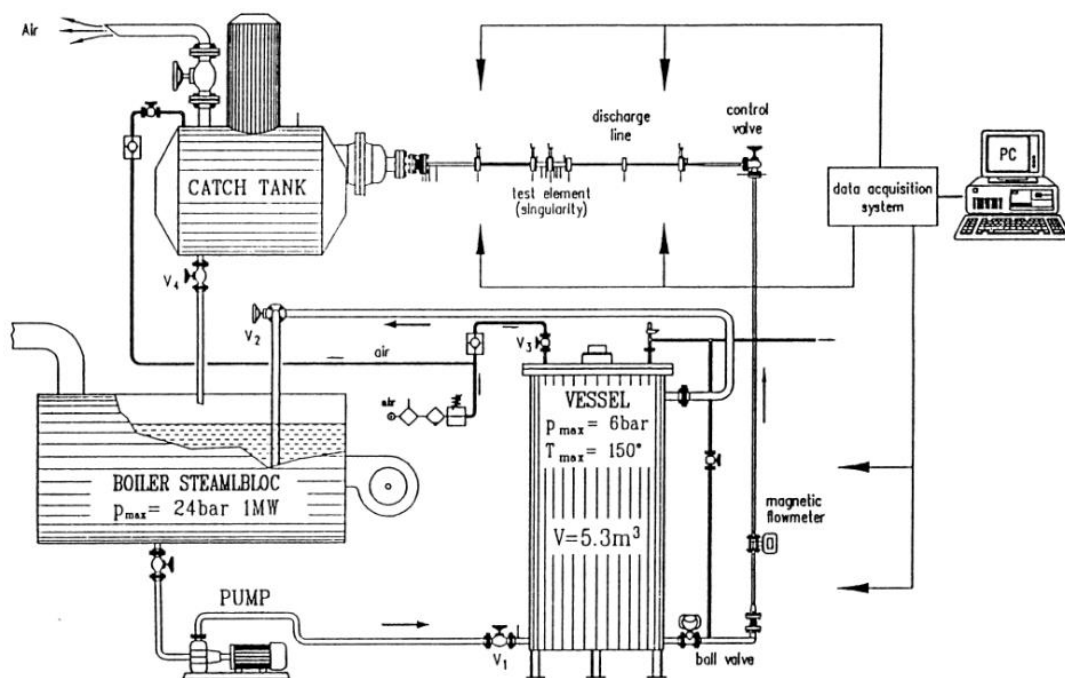


Figure 16: Experimental test facility (Attoul et al., 2000)

Initial compressed air was used to fill the downstream tank, and a valve on the exhaust pipe was used to regulate back pressure. A discharge line that was made up of a ball valve, a vertical pipe, a manual control valve, and a horizontal test section connected the upstream and downstream vessels to one another. The test section's two distinct geometrical arrangements were investigated. In the first, a horizontal pipe with a diameter of 0.0284 m included a circular aperture with a diameter of 0.017 m or 0.020 m. The length of the horizontal pipe was recorded as 2.8 m, giving a L/D ratio of about 100. The opening was in

the centre of the horizontal pipe. As part of the alternative geometrical design, an abrupt expansion was implemented. This design included an upstream pipe measuring 0.017 m in diameter and 1.4 m in length, giving an L/D ratio of about 80 in the upstream, as well as a downstream pipe measuring 0.0284 m in diameter and 1.4 m in length. Pyrex glass test section tubes were utilized to observe and visualize the flow patterns in the vicinity of the sudden cross-sectional area shift. An electromagnetic flowmeter was used to gauge the mass flow rate at the vertical pipe's base. Due to a maximum temperature of 150 °C, the flowmeter restricted the upstream circumstances. Using five chromelalumel thermocouples, the temperature was monitored. A manual control valve and a catch tank were two of the three locations where temperature readings were taken in the test portion. In total, 19 sites had their pressures checked. Local void fraction and axial bubble velocity at the flow axis were monitored using a twin optical probe called BS1 that was placed 2 mm from the upstream pipe's outlet (Attoul et al., 2000).

The upstream and downstream vessels of the experiment were initially under the same pressure. Once air pressure and critical flow conditions were reached, the downstream pressure was gradually decreased. After this step, the manual valve was adjusted to reach the necessary pressures (which ranged from 0.5 MPa to 0.15 MPa) at the entry of the test area. Between 0 and 14 degrees Celsius were subcooled at the entry. Figure 17 illustrates how the double-choked critical flow occurred (Attoul et al., 2000).

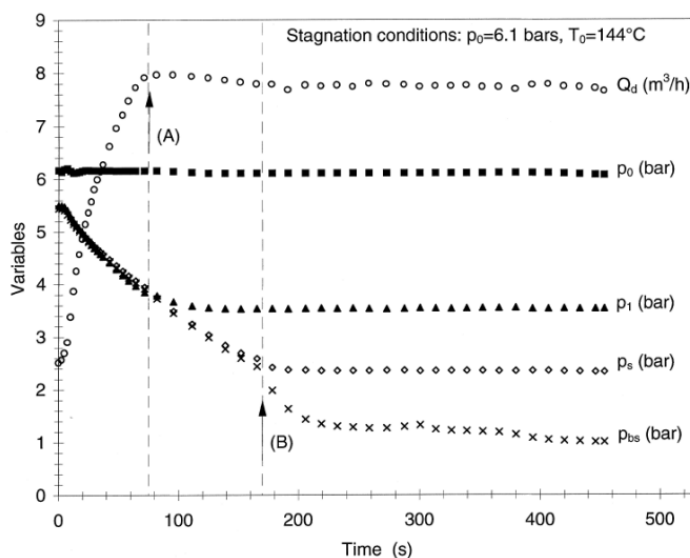


Figure 17: Double-choked critical flow, evolution of the flow variables during the decrease of the backpressure: sudden enlargement, small stagnation subcooling $\Delta T_{sat,0} = 9$ °C (A. Attoul et al., 2000)

In the test part, viewing of choked flow patterns was also made feasible using Pyrex pipes. Figure 18 shows the choked flow pattern for significant subcooling at the intake (Attoul et al., 2000).

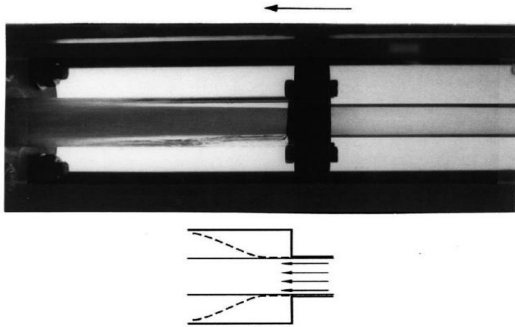


Figure 18: Confined quasi free jet pattern (Attou et al., 2000)

At the intake, the temperature was 120.8 °C and the subcooling was 12.3 °C, 0.296 MPa of pressure and 0.135 MPa of back pressure were present. With a mass flow rate of 11.12 m³/h, the flow was blocked. The core flow was seen to be conical with a short opening angle in the axisymmetric restricted quasi free jet pattern. Figure 19 shows the constricted flow pattern for liquid close to saturation point with inlet subcooling of 1.1 °C (Attoul et al., 2000).

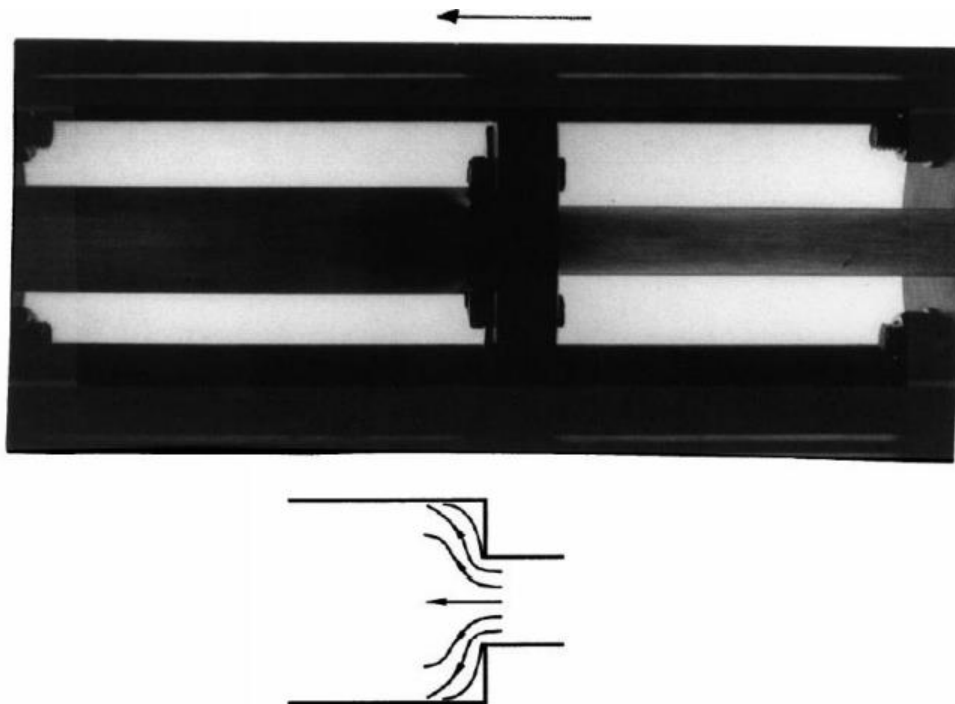


Figure 19: Expanded jet pattern (Attoul et al., 2000).

The test loop's components are as follows: 1. Water tank, 2. Control valve, 3. Filter, 4. High pressure plunger pump, 5. Orifice, 6. Regenerative heat exchanger, 7. Heat exchanger, 8. Electrode, 9. Pressure vessel, 10. Connection tube upstream of the break nozzle, 11. Break tube section, 12. Shutoff valve, 13. Coiled copier heat exchanger, 14. Expansion tube, 15. Load cell, 16. Water collection tank (Xu&Wang, 1999).

The high-pressure plunger pump was utilized to pressurize the feed water (4) and divided into two circuits, one stream was directed through the bypass to modify the mass flow rate and pressure of the loop, while the other stream passed through orifices into the heated section (8), which had an inner diameter of 16 mm. Via the heated part, the fluid entered the pressure vessel (9) while being subcooled in a controlled manner. The 0.125 m³ pressure vessel had a volume. The upstream tube (10) with a diameter of 20 mm and the break tube section (11) with a diameter of 4 mm and various lengths both received the subcooled water when it emerged from the bottom of the pressure vessel. The experiment program included five various tube lengths (Xu&Wang, 1999).

An optical technique was used to measure the diameters of the break section tubes. After the appropriate subcooling and system pressure were attained, the cut-off valve (12) was opened to allow the discharge into the water collecting tank (16) through the expansion tube (14) with a diameter of 30 mm. The collection tank's coiled copy heat exchanger cooled the water-steam combination that had been released (13). The mass flow through the break test portion was monitored using two load cells (15). Using two orifices (5) for measurement and valves A and B for control, the circuit's mass flow rate was determined (Xu&Wang, 1999).

NiCr-NiSi jacket thermocouples were used to measure the fluid temperatures along the heated tube as well as at the pressure vessel's inlet and outflow as well as in the break test section. The liquid level in the pressure vessel was measured using differential pressure transducers, while the pressures in the break test area were monitored using pressure gauges. A 0.5 mm upstream measurement of the tube exit pressure was made. This was considered by the authors as the critical pressure for the p_c/p_0 critical pressure ratio. Figure 21 displays the critical mass rate in relation to the L/D under saturated conditions (Xu&Wang, 1999).

When the upstream pressure drops, the critical mass flow rate falls. The critical mass flow rate clearly depends on the L/D ratio. Comparatively, smaller L/D has a greater critical mass

flow rate. Figure 22 shows the impact of upstream subcooling with various L/D ratios at 4.0 MPa upstream pressure (Xu&Wang, 1999).

Examining Figure 21 reveals that as the L/D ratio increases, there is a consistent reduction in the critical mass flux. L/D dependence fades on Figure 22 and Figure 23 when the subcooling increases. Apparently at the range of tested L/D's, once the subcooling exceeds 30 °C or so, there is little to no flashing before the throat. Flashing retards, the flow. The authors concluded that the upstream pressure is the governing factor for the critical mass flow rate and that liquid flashing may be disregarded due to the liquid's brief transit in short tubes. Due to flashing at the break test section before the exit, the smaller subcooling has a visible impact on the critical mass flow rate when $L/D > 4.96$. Figure 23 present the impact of subcooling and L/D for upstream pressure of 16 MPa (Xu&Wang,1999).

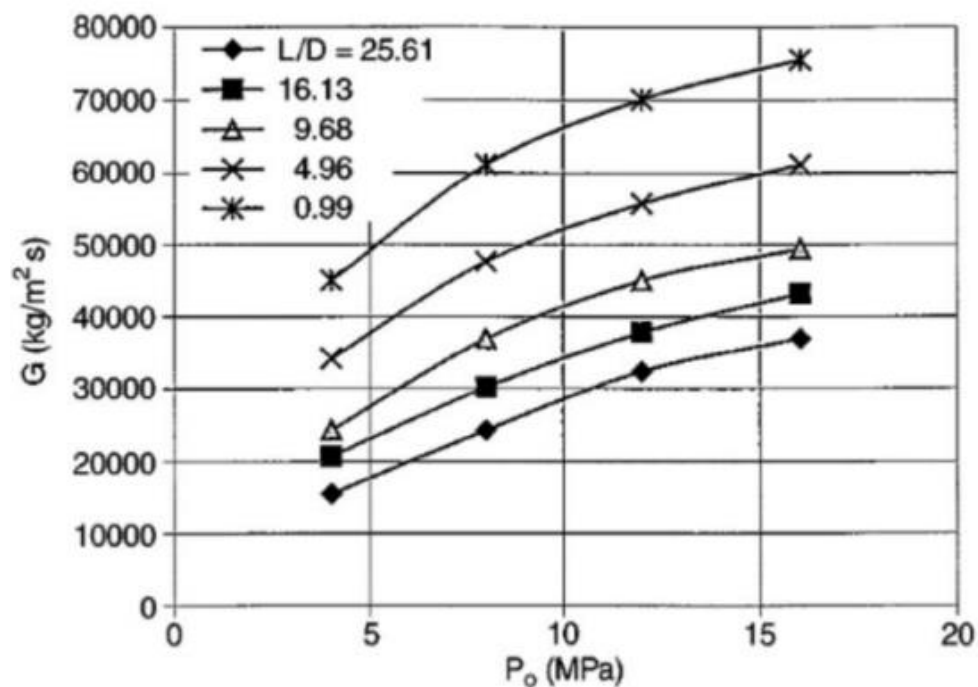


Figure 21: Critical mass velocity versus upstream pressure (Xu&Wang, 1999)

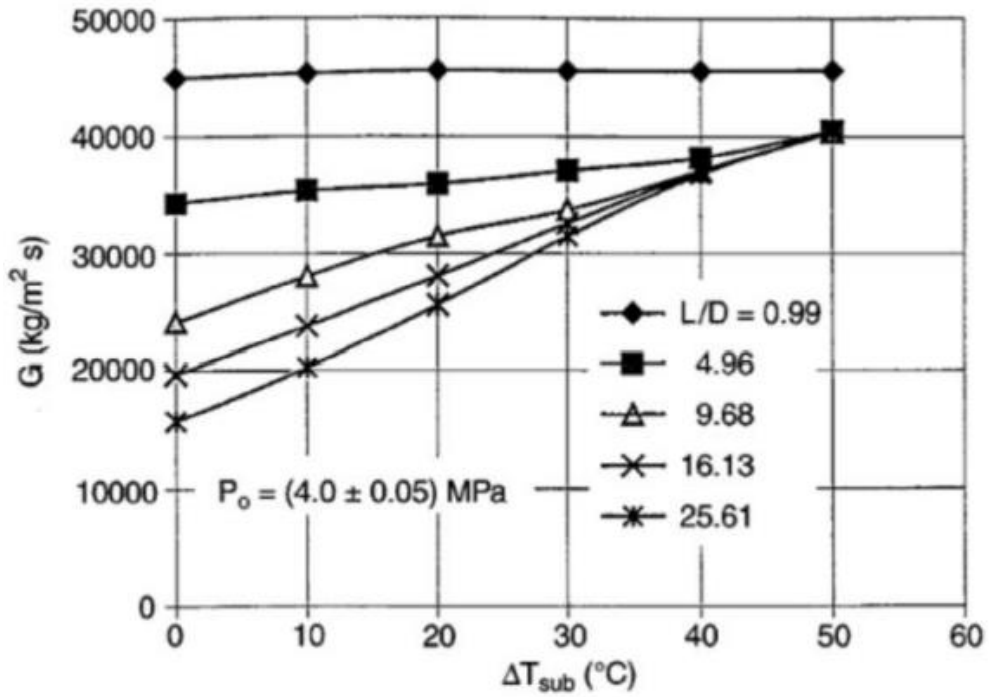


Figure 22: Critical mass velocity versus upstream liquid subcooling (Xu&Wang, 1999)

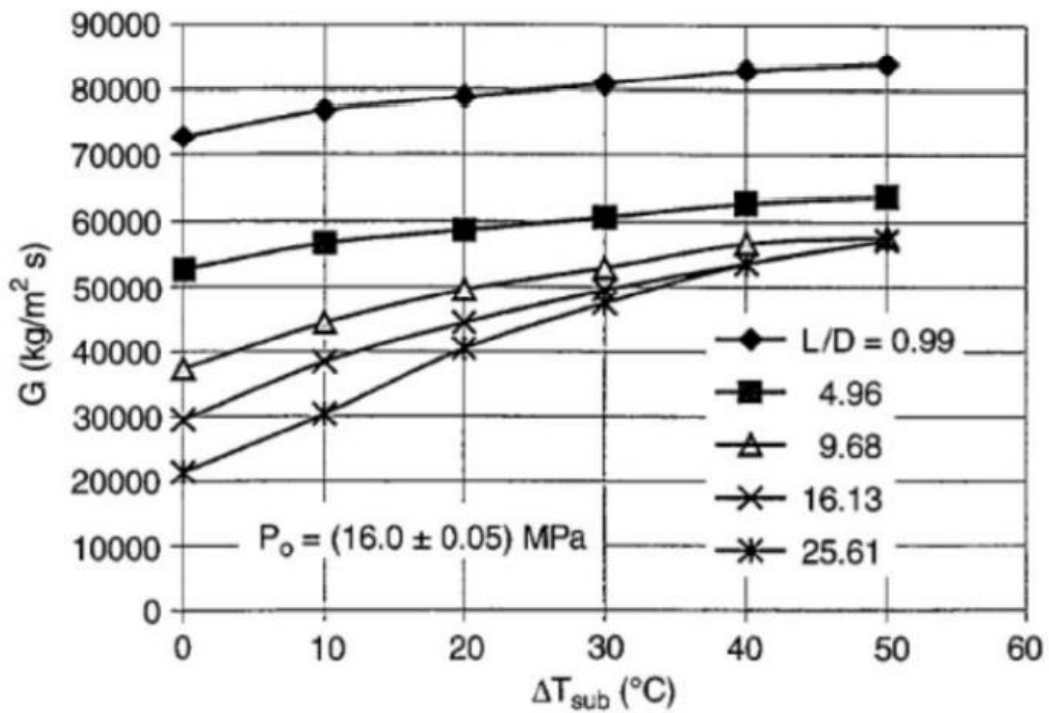


Figure 23: Critical mass velocity versus upstream liquid subcooling (Xu&Wang, 1999)

When the upstream pressure is increased to 16 MPa from the prior upstream pressure of 4 MPa, the L/D ratio of 4.96 likewise appears to decouple from the higher L/D ratios. With an L/D ratio of 0.99, the critical mass flow rate decreases as the upstream temperature approaches saturation, indicating that some flashing may occur at high pressure as the upstream condition approaches saturation (Xu&Wang, 1999).

3.6 A metastable jet model for leaks in steam generator tube.

Heckmann et al., conducted an experimental investigation of a steam generator tube leak in 2022. PRISE leaks are brought on by steam generator tube leaks. Detecting small leaks anywhere in the primary system is an integral part of the leak-before-break (LBB) concept. The future expansion or rupture can be stopped if a tiny leak can be found. The leak rate plays a significant role in measuring the release of activity per unit of time for postulated leakages, as it represents a fraction of the mass flow rate through a breach. (Heckmann et al., 2022).

The trials were conducted at the MPA University of Stuttgart's modular fluid-structure-interaction (FSI) test facility. In FSI, a leak rate up to 200 g/s can be detected. FSI permits measurements at pressures ranging from 0.2 MPa to 7.5 MPa and temperatures ranging from room temperature to 270 °C. Figure 24 present the FSI test lab (Heckmann et al., 2022).

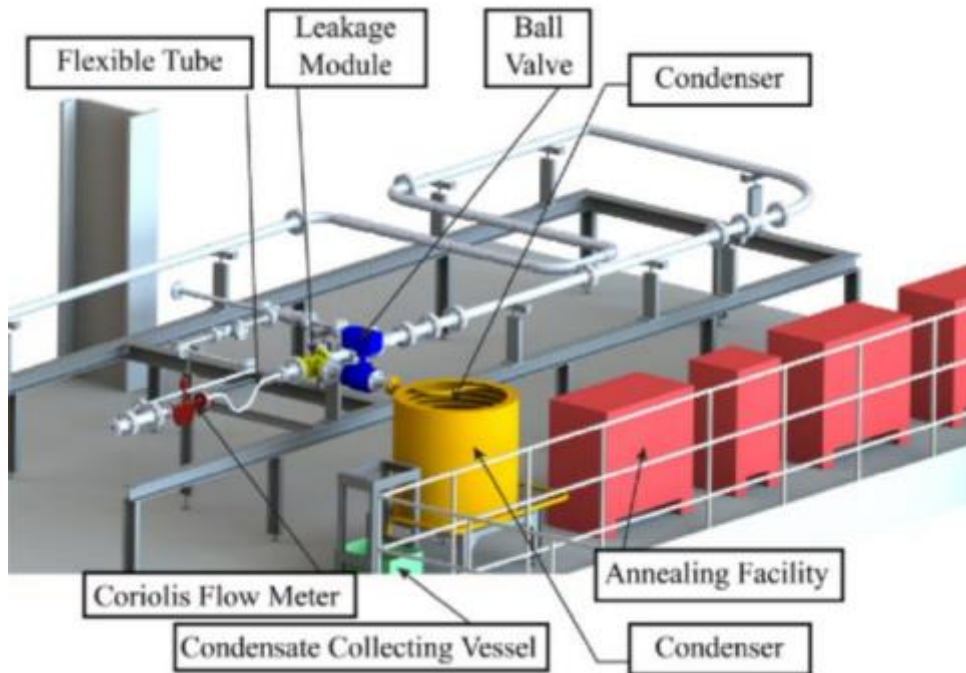


Figure 24: FSI test rig (Schimid et al., 2021)

A membrane plunger pump is used to pressurize the test facility's cold pipe system, and a hermetic centrifugal pump is used to pressurize the hot main loop. An annealing system in the pipe system, with a power of 300 kW, is used to achieve the appropriate temperature. Using a Coriolis flow meter, mass flow may be assessed at three points. The mass flow rates of the leak can be determined using a calibrated load cell fitted to the condensate collecting vessel or a Coriolis flow meter upstream and downstream of the leak. Because of the greater projected accuracy, load cell measurement was selected. To analyse visually the exit flow regime using high-speed imaging, the test rig was changed. High-speed camera, H; leakage module, L; optical observation chamber, O; leakage collection vessel, V; and Coriolis flow meter, C are the key elements in Figure 25. The three fundamental outflow patterns that were identified include a pure water jet, a free water jet combined with a wet steam cone, and a pure wet steam cone. In Figure 26, the outflow patterns are shown. At water temperature and pressure ranges, the flow patterns were seen. At a temperature of 125 °C and a pressure of 4.7 MPa, the observed outflow pattern was a pure water jet. At a temperature of 151 °C and a pressure of 1.3 MPa, a combination of a free water jet and a steam cone was observed. Finally, at a temperature of 200 °C and a pressure of 4.1 MPa, a pure wet steam cone. When the outflow regime was examined visually, the mass flow rates were not measured (Heckmann et al., 2022).

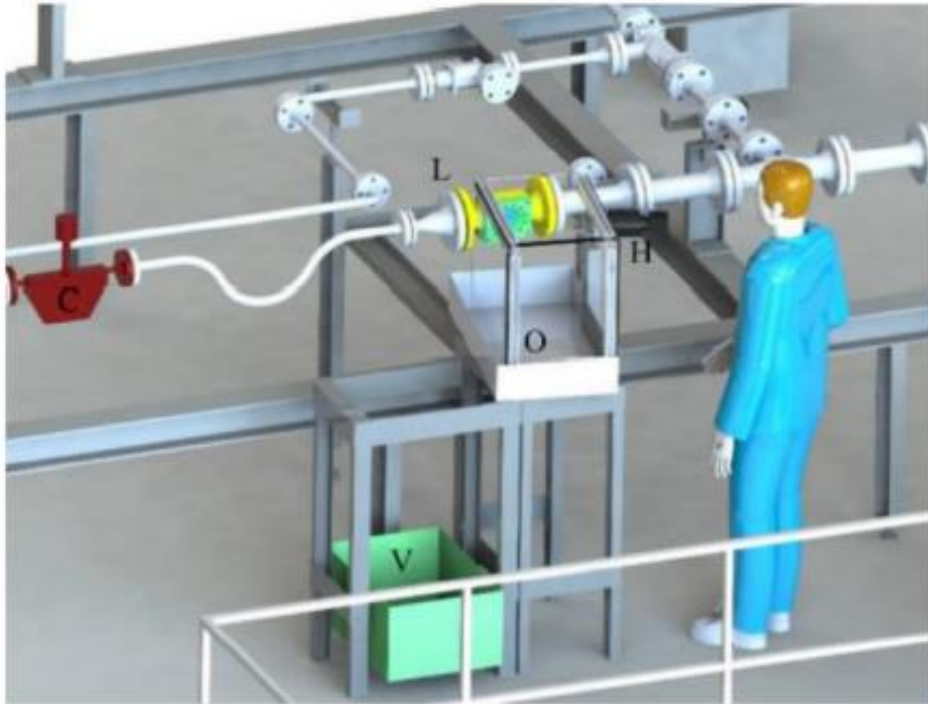


Figure 25: Setup of the FSI Test rig (Heckmann et al., 2022)



Figure 26: Examples for specific flow patterns: Jet only (left), jet and steam cone (center) and steam cone only (right) (Heckmann et al., 2022).

While using PRISE, subcooled liquid flows from the main side to the secondary side, where the water is completely saturated. The test facility Figure 27 was altered to examine the impact of using water instead of air on the outer side. The water vessel had a spill over mechanism (S) attached to it, and a leakage collecting vessel (V) was used to catch the leaking. Figure 28 shows the leakage rate data for discharge into air and water (Heckmann et al., 2022).

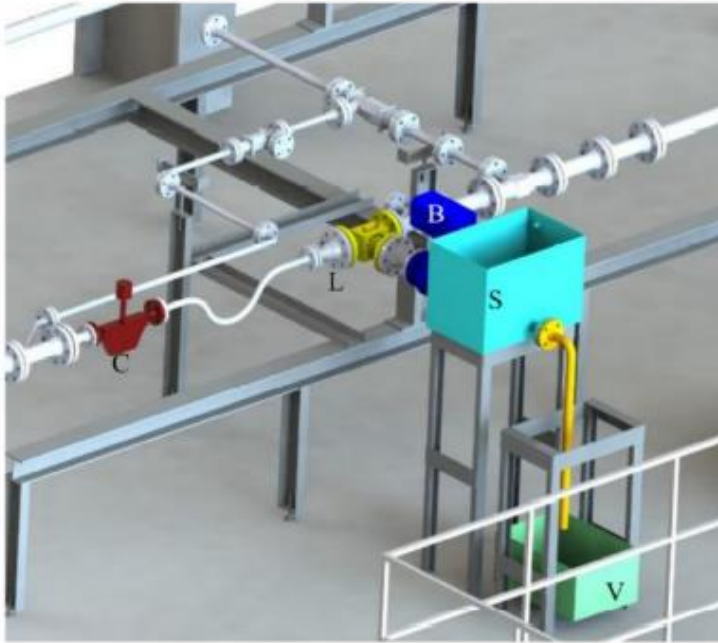


Figure 27: Setup of the FSI test rig for leak rate measurement with discharge into a water vessel (Heckmann et al., 2022)

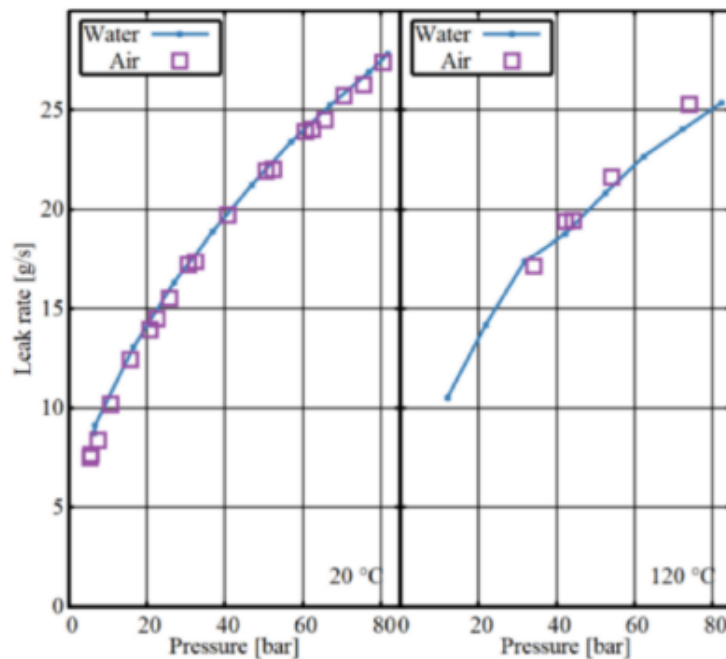


Figure 28: Leak rate values for discharge into water and air (Heckmann et al., 2022)

20 °C offered good uniformity. The disparities at 120 °C are caused by partial condensation of the leakage and overflow device heat-up, according to the authors. There was no description given of the circumstances within the water vessel (Heckmann et al., 2022, 4)

3.7 A study of subcooled choked flow in real steam generator tube cracks.

In 2019, Revankar and Riznic presented the experimental findings of a stress corrosion crack (SCC) on the steam generator tube that restricted the flow of originally subcooled water. Axial SCC was used to analyze five different samples. CANDU steam generator artifacts made up three of the samples (samples 1, 2, and 4). Two samples (samples 3 and 5) that looked like the steam generator tubes from a US PWR were retrieved from a study effort on SG integrity at Argonne National Laboratory. Figure 29 shows where the testing will take place (Revankar&Riznic, 2019, 3).

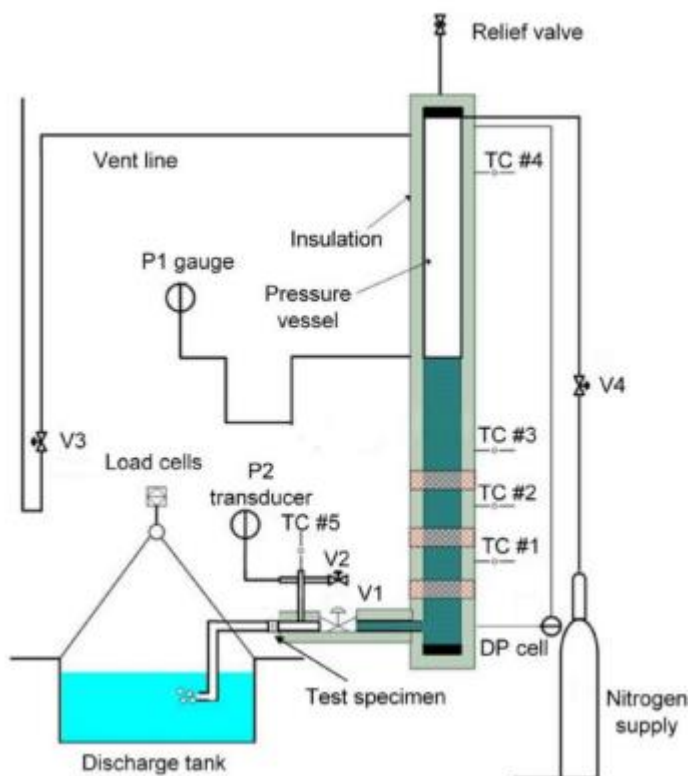


Figure 29: Schematic of the test facility (Revankar&Riznic, 2019)

The pressure vessel, test section, where the specimens were mounted, and discharge tank made up the test facility's primary parts. A single 90 mm-diameter seamless pipe was used to build the pressure vessel. Different upstream stagnation conditions were achieved by pressurizing the pressure vessel with nitrogen and heating it with ceramic band heaters. A discharge tank was filled with the test specimen's discharge after it had been collected. K-type thermocouples were used within the vessel and before the test specimen to detect temperature. The midline of the flow was where all the thermocouples were put. A needle

gauge (P1) was used to monitor the vessel pressure, and a differential pressure transducer to measure the water level (Revankar&Riznic, 2019).

Incoloy 800 tubes with a wall thickness of 1.2 mm and an outer diameter of 15.9 mm constituted Samples 1 and 2. Sample 4, on the other hand, featured an Inconel 600 tube with a wall thickness of 1.1 mm and an outer diameter of 12.7 mm. Inconel 600 tubes with a wall thickness of 1.3 mm and an outer diameter of 22.2 mm were used for samples 3 and 5. Synthetic axial fractures were intentionally created in these particular samples. The sample tubes were cut so that the centre of the tube was left cracked. On one end, the tube was welded to a fitting, and on the other, a stainless-steel disc was used as a cap. This made sure that just the fracture was used to release the fluid. Figure 30 presents the test specimens (Revankar&Riznic, 2019).

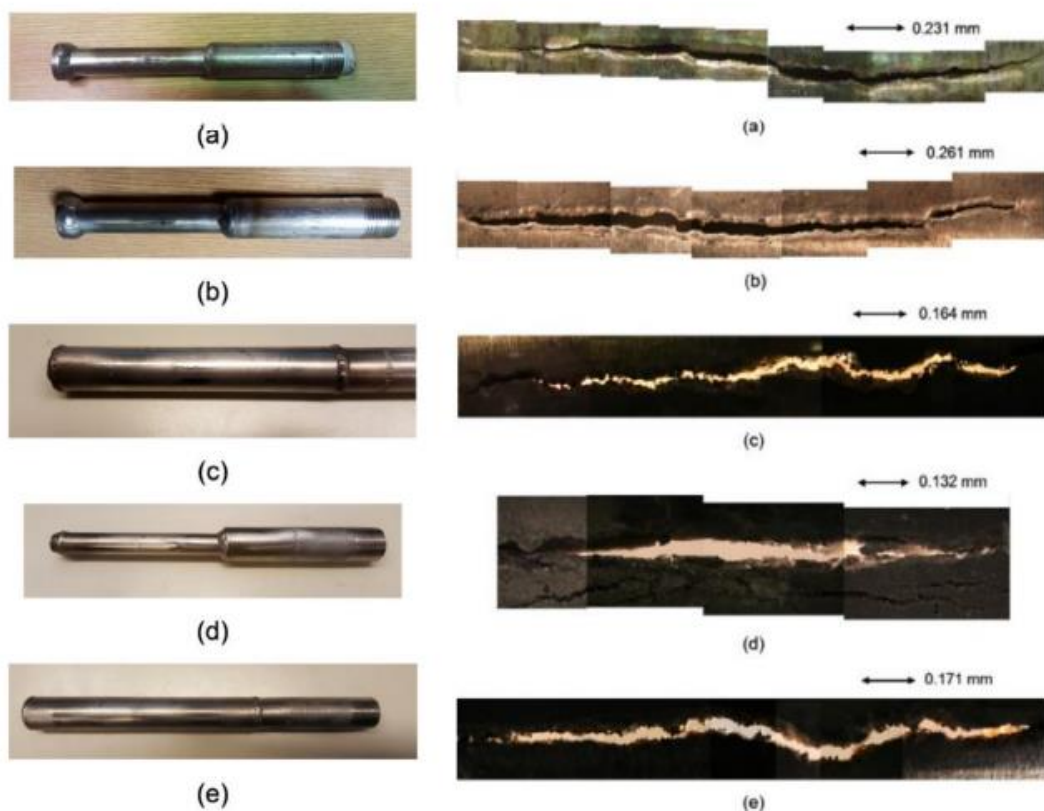


Figure 30: Steam generator tube samples and cracks (Revankar&Riznic, 2019)

Figure 31 shows the findings of an investigation into the mass flux through several specimens at room temperature and in subcooled conditions with various stagnation pressures (Revankar&Riznic, 2019).

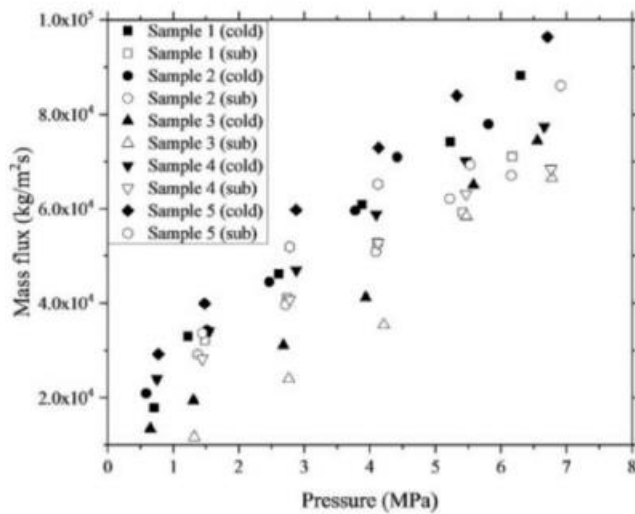


Figure 31: several specimens at room temperature and in subcooled conditions with various stagnation pressures (Revankar&Riznic, 2019)

The subcooling level was not indicated by the authors, however it was inferred from published data that it was 40 °C. The choking effect may be seen since the discharge mass fluxes at room temperature are higher than one might anticipate. L/Ds impact was also investigated. One more sample from John et al., with an L/D of 72 was used for comparison because the samples' L/Ds ranged from 1.9 to 6.1 (Revankar&Riznic, 2019). The comparison's findings are shown in Figure 32.

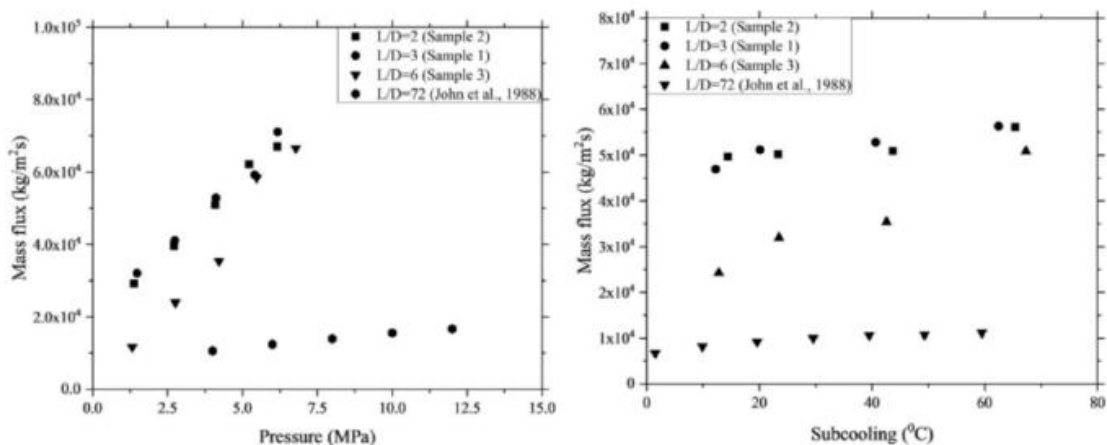


Figure 32: Comparison subcooled flashing discharge mass flux at different L/Ds with mass fluxes versus liquid subcooling at stagnation pressure approximately 4.14 MPa (Revankar&Riznic, 2019).

The rise in L/D resulting from the increase in channel length has a significant impact on the position of the flashing, as stated by the authors. The rapid depressurization rate experienced by liquid flowing through a narrow tube leads to overheating and a delay in flashing. Friction has a considerable impact on the choked flow because of the dependency of mass flux on L/D (Revankar&Riznic, 2019).

3.8 Summary on the two-phase critical flow modelling

In the summary report by Pyy (2022) the following was concluded: comprehensive literary examination of current critical flow experimentation the maximum upstream pressure ever utilized was 16 MPa. As it is more than in the standard critical flow tests, it can provide novel information. Actual steam generator fractures rather than manufactured ones were used in the experiment in Revankar, S.T., Assessment of Leak Rates through Steam Generator Tubes, which also provided interesting novel information. Instead of releasing the upstream liquid-gas mixture into another downstream vessel with gas atmosphere, in the Heckmann, K. et al., A metastable jet model for leaks in steam generator tubes dumped it into the water directly, which is the situation in the real PRISE scenario. In the literature review, there are no previous experiment investigations where such a discharge setup has been used.

When it comes to validating various SYS-TH codes, the traditional critical flow tests are still useful. The CSNI validation test matrix, which maps out best SETs for critical flow studies prior to 1993. The CSNI validation matrix has not been updated in almost three decades. The FONESYS benchmark, in which all the main SYS-TH developers took part Landfredini, M. et al., Critical flow prediction by system codes – Recent analyses made within the FONESYS network (Landfredini et al., 2020), used the experiment described in Attou, A. et al., Experimental study of the critical flashing flow through a relief line: evidence of the double choked flow phenomenon (Attou et al., 2000). This leads to the conclusion that the traditional critical flow tests are still highly state-of-the-art. This is especially true for the Marviken experiments, which remain the only full-scale critical flow tests with a large diameter pipe and a high upstream pressure of 5 MPa.

Modern experimentation would need to generate the following measurement data in order to be truly beneficial for model building and validation: mass flow rate, pressure variation along the axial direction of the break test section $P(z)$, evolution of void fraction along the same direction (z), and liquid temperature evolution along that axis: As the annular-mist flow transitions to pure mist flow, the slip ratio, bubble size or at least bubble size at detachment, and the development of the liquid mass flowrate and void percentage may all be calculated by the integration of the liquid energy equation and the liquid temperature. droplet size, droplet velocity, and film thickness.

The utilization of high-speed imaging, along with pattern recognition techniques, infrared thermometry, and other complementary methods, has the potential to facilitate the acquisition of certain essential information. These techniques can assist in capturing data such as bubble behaviour, flow patterns, temperature distribution, and other relevant parameters, contributing to a more comprehensive understanding of the system under investigation. It is not appropriate to use invasive techniques since they will affect the critical flow rate (Bestion et al., 2023).

4 C-FLOW Separate-Effect-Test Facility.

This section provides an overview of the C-FLOW Separate-Effect-Test Facility, explaining its structure, design, and operational procedures.

The test facility consists of an upstream pressure vessel, U-shaped pipeline with a volumetric flow measurement device, a quick-acting valve, and a changeable discharge tube part that acts as the actual test bench. These discharge tubes with different L/D ratios and diameters will be attached to the quick-acting valve.

During the operation of the facility, the purpose is to release subcooled or saturated water into the atmosphere through the tube, during which the pressure profile is measured from the pipe with an impulse line.

The maximum pressure of the pressure vessel is 10 MPa, and the maximum water temperature is 270 °C. The intention was to use the SCRAM tank already existing in LUT

as an upstream pressure vessel. The original idea would be to connect a tube with an L/D ratio up to or larger than 350 to the measuring tube. Figure 33 present 3D model of the SET at the time of writing the thesis.

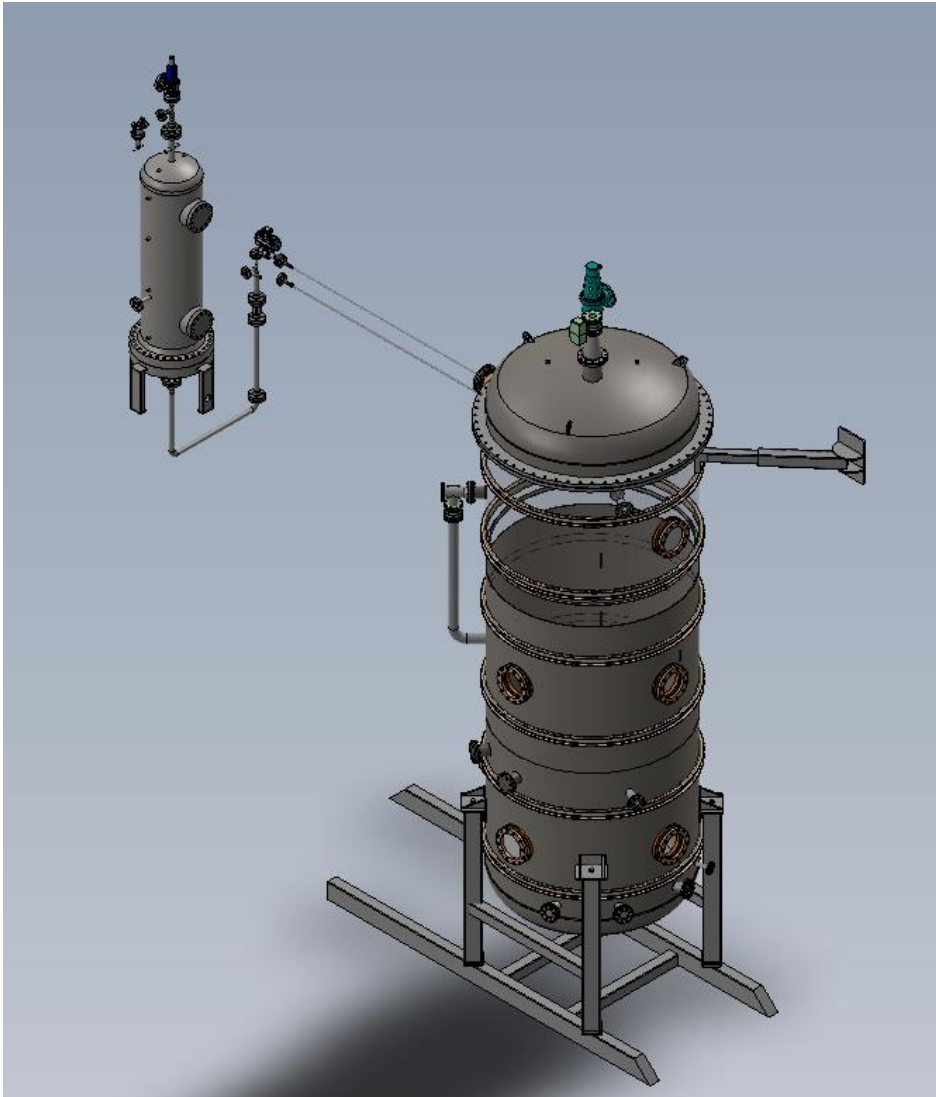


Figure 33: C-FLOW separate-effect-test facility (C-FLOW SET 3D model revision v.1)

4.1 Design of C-FLOW test facility

The upstream pressure vessel has a capacity of 0.74 m^3 . The vessel acts as a reservoir for pressurized hot water that is released to the actual test bench part. The maximum pressure that can be used in pressure vessel is 10 MPa. The tentative plan is to use nitrogen or

compressed air for pressurizing pressure vessel, but this is subject to further clarification and depends on how and what gas can be conveniently obtained, as it will be consumed in enormous quantities.

At the bottom of the pressure vessel, there is a DN65 outlet connection (inner diameter of 64 mm), from which subcooled water flows out of the vessel through a "measurement pipe", that is a U-shaped pipeline. This DN65 pipe is 535 mm long and joins a DN50 pipe (inner diameter of 49 mm) with suppression cones. The pipe including the cone is 889 mm long before the first 90-degree bend.

The measurement pipe continues as a U-shape with two DN50 curves, and the distance between the centrelines is 1340 mm. After the U-bend, there is 1000 mm of DN50 pipe before the flow meter.

After the vortex type flow meter, there is a straight section of DN50 pipe, 250 mm in length, which leads to a T-junction. Water with temperature depending on the experiment needs is taken from PACTEL facility. The preheating water first enters the upper part of the pressure vessel. From T-junction the heating water is run back to PACTEL. The C-FLOW test facility and PACTEL form the heating circuit.

The circuit is cut off with valves before the blowdown experiment begins. The maximal temperature of water in this experiment is 270 °C, which is about 40 °C sub-cooling. After the T-junction, there is a curved section before the valve, which is DN25 and has convergent cones before and after it. The changeable discharge tube is connected to the pipe after the control valve.

The inner diameter of the discharge tube is near either the Loviisa/VVER-440 or Olkiluoto 3 / EPR steam generator tube diameter. In Loviisa VVER-440, the inner diameter of the steam generator tube is 13.2 mm and in Olkiluoto EPR tube diameter is 16.87 mm. The discharge tubes in the facility are planned to have an inner diameter of 13 or 17 mm. The discharge tube leads to PPOOLEX facility, with ambient air pressure. Tentative 3D image of the C-FLOW test facility can be seen from the Figure 34.



Figure 34: C-FLOW test facility main components (C-FLOW test facility 3D model revision v.1).

5 Apros simulation model of C-FLOW test facility for two-phase critical flow study

5.1 Apros code

A simulation model of the C-FLOW SET facility has been developed using Apros v6.08. Apros is a computer simulation tool specifically designed for modelling thermal hydraulic processes in both nuclear and conventional power plants. By utilizing Apros, the simulation model aims to accurately replicate and analyse the thermal hydraulic behaviour within the C-FLOW facility, providing valuable insights into the system's performance and behaviour

under various operating conditions. At present, VTT and Fortum Ltd share ownership and jointly engage in its development. Apros includes multiple techniques for calculating two-phase flow (e.g., liquid water and steam) based on the required precision level: homogeneous model, 5-equation (drift-flux) model, and 6-equation model (Kurki et al., 2019).

The utilization of the 6-equation model, regarded as the most advanced among Apros' flow models, is employed in this study. Rather than relying on assumptions concerning the characteristics of the two-phase flow, the 6-equation model computationally determines the necessary parameters to describe a system containing gas and liquid phases. These parameters include pressures, void percentage, enthalpies, and velocities, which are calculated separately for each phase (Kurki et al., 2019).

The foundation of Apros's six-equation solution system revolves around the utilization of one-dimensional conservation equations for mass, momentum, and energy. The system incorporates a total of six partial differential equations when applying the equations for both the liquid and gas phases (Kurki et al., 2019). The equations take the following form Eq. (73) conservation of mass, Eq. (74) conservation of momentum, Eq. (75) conservation of energy.

$$\frac{\partial(\alpha_k \cdot \rho_k)}{\partial t} + \frac{\partial(\alpha_k \cdot \rho_k \cdot u_k)}{\partial z} = \Gamma_k \quad (73)$$

$$\begin{aligned} \frac{\partial(\alpha_k \cdot \rho_k \cdot u_k)}{\partial t} + \frac{\partial(\alpha_k \cdot \rho_k \cdot u_k^2)}{\partial z} + \alpha_k \cdot \frac{\partial P}{\partial z} \\ = \Gamma_k \cdot u_{ik} + \alpha_k \cdot \rho_k \cdot \bar{g} + F_{wk} + F_{ik} + F_{va} + F_{fl} + \Delta p_{pu} \end{aligned} \quad (74)$$

$$\begin{aligned} \frac{\partial(\alpha_k \cdot \rho_k \cdot h_k)}{\partial t} + \frac{\partial(\alpha_k \cdot \rho_k \cdot u_k \cdot h_k)}{\partial z} \\ = \alpha_k \cdot \frac{\partial p}{\partial t} + \Gamma_k \cdot h_{ik} + Q_{ik} + Q_{wk} + F_{ik} \cdot u_{ik} \end{aligned} \quad (75)$$

where, k is subscript, that refers to liquid or gas.

i is subscript, that refers to interface.

w is subscript, that refers wall.

F is subscript, that refers to friction force.

Q is subscript, that refers to heat flow.

va is subscript, that refers to valve friction.

fl is subscript, that refers to friction from form loss.

pu is subscript, that refers to pump head.

In the six-equation model, the gas phase can encompass non-condensable gases as well. In this work, non-condensable gases are included to establish the initial conditions. The non-condensable gas is assumed to persist in the gas phase throughout the simulation. The model does not take into account the dissolution of the non-condensable gas in the liquid phase. Furthermore, non-condensable gas and steam are supposed to create a homogenous mixture with the same temperature and velocity (Kurki et al., 2019).

Based on the aforementioned assumptions, along with the standard conservation equations of the six-equation model, only the mass conservation equation for the non-condensable gas is necessary (Hänninen et al., 2012). The equation for non-condensable gas mass is:

$$\frac{\partial(\alpha_g \cdot \rho_n)}{\partial t} + \frac{\partial(\alpha_g \cdot \rho_n \cdot u_g)}{\partial z} = 0 \quad (76)$$

where, n is subscript, that refers to non-condensable.

In Apros, the calculation of state variables, such as pressure and void fraction, occurs within designated control volumes called nodes. On the other hand, vector values like velocity are determined in control volumes positioned between nodes, referred to as branches. Each branch connects two nodes. This configuration of control volumes is commonly referred to as a staggered grid (Hänninen et al., 2012).

In Apros The isentropic expansion assumption for single-phase liquid, a user-selectable correlation for two-phase flow (currently the Moody or Henry-Fauske model), and the ideal gas assumption for steam are used to calculate the critical mass flow rate (choking) (Kurki et al., 2019).

Choked flow models are often developed on the premise that the input to the critical flow section consists of a huge reservoir with static conditions. Stagnation conditions should be employed when using such a model in a situation where the upstream flow conditions are not static. The inlet thermodynamic conditions should be examined at this stationary stage for the choked flow models to behave correctly (Kurki et al., 2019).

In the event of two-phase flow, the critical mass flow rate is calculated using a correlation chosen by the user (Kurki et al., 2019). In this work, modified Moody model is used in simulation. The modified Moody model incorporates more advanced correlations and equations that consider for example factors such as the compressibility of fluids and the presence of non-condensable gases. These factors hold significant relevance in two-phase flow systems where non-condensable gases are present. The available options are presented in Table 1.

Table 1: Critical mass flow rate correlations (attribute TH6_CRIT_FLOW_MODEL of the module type TH6_CONTROL)

Options	Correlation
1	Moody model (polynomial fit) with node average pressure used for defining the critical flow
2	Henry-Fauske model (iterative solution) with node average pressure used for defining the critical flow
3	Moody model (old, less accurate polynomial fit, not recommended) with node average pressure used for defining the critical flow
4	Moody model (polynomial fit) with stagnation pressure used for defining the critical flow
5	Henry-Fauske model (iterative solution) with stagnation pressure used for defining the critical flow
6	Moody model (old, less accurate polynomial fit, not recommended) with stagnation pressure used for defining the critical flow

5.2 Simulation model

The created simulation model of the C-FLOW SET facility is presented in Figure 35. The initial conditions of the simulation: the pressure vessel and U-loop pipeline are filled with water, while pressurized air is continuously supplied from the top of the vessel, maintaining a constant pressure of 10 MPa throughout the experiment. The flow meter is replaced by a pipe component with identical dimensions (diameter and length) to that of a flow meter. The control valve is set to a closed position at the beginning of the simulation. The water within the pressure vessel is set to a temperature of 270 °C. The discharge tube is initially filled with air at a pressure of 0,1 MPa and a temperature of 29 °C. The model offers six different lengths of discharge pipe, each with its own L/D ratio. The model has tested each of these separate discharge tubes separately.

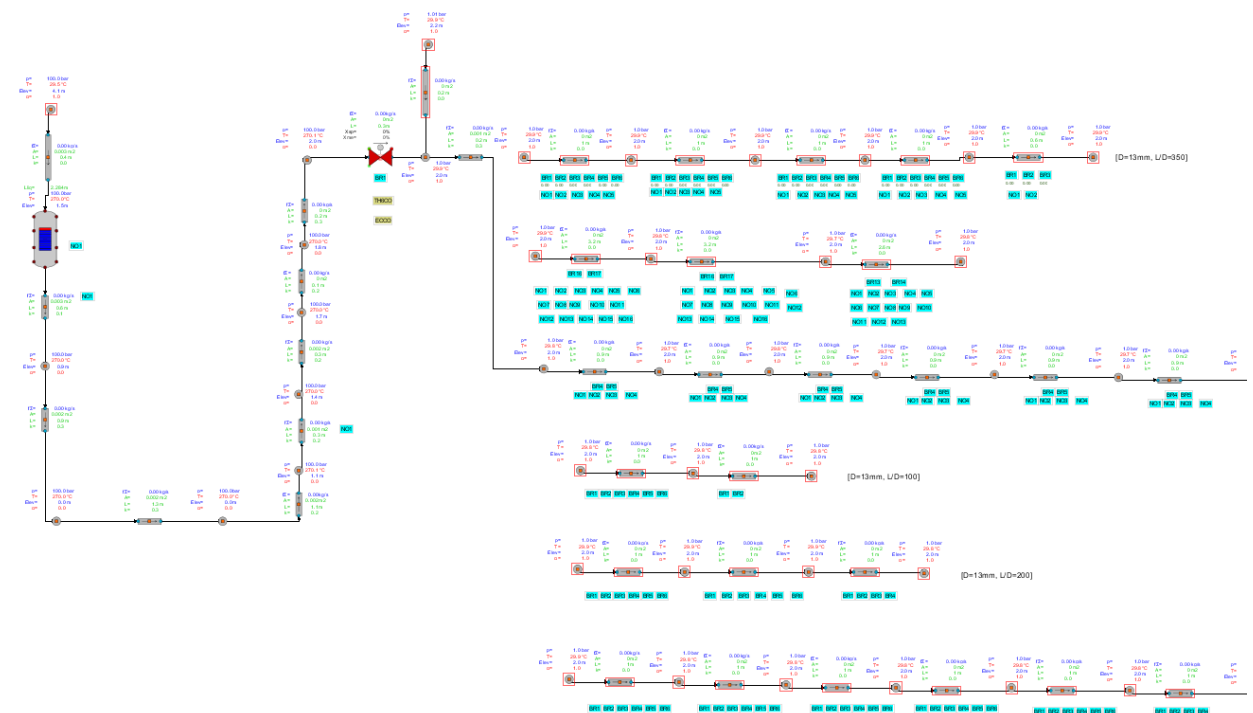


Figure 35: Apros simulation model of the C-FLOW test facility (Apros).

Moving beyond the U-loop, to the main line can be connected to a range of discharge tubes that have distinct length-to-diameter (L/D) ratios. In each individual simulation case, a specific discharge tube will be chosen and attached to the main line. These discharge tubes simulate the steam generator tubes found in power plants like Loviisa VVER-440 and

Olkiluoto EPR. The simulation model uses the discharge tube inner diameters of C-FLOW test facility (13 mm & 17 mm).

When the simulation begins, the control valve remains closed, allowing the system to stabilize. It took in average 10-20 seconds to once the conditions have reached a steady state situation. Then, the control valve was opened to initiate the flow. The valve was set to open in 1 second. As the valve was fully open, the flow gradually developed, and the observation and analysis of the test facility was enabled.

The simulation concluded when the pressure vessel, initially filled with water, become empty. At that point, the pressure vessel contained only air, and the liquid is discharged to the atmosphere through the designated discharge tube.

The L/D ratios considered in this study were 10, 50, 100, 200, 350, 500, and 700. Critical flow checking was enabled for all tubes within the simulation model, not only in the discharge tube, which is the focus of the research. In the simulation, the code predicted a critical flow at the end of the discharge tube (in the last branch). The discharge coefficient employed in the discharge tube corresponded to the default value specified by the code, which was 0,75. Within the simulation model, the tubes are discretized into nodes, allowing for detailed analysis of the system's behaviour. Each node has a fixed length of about 0.2 meters, enabling precise calculations and tracking of parameters along the tubes. In instances where the tube's length is less than 0.2 meters, there will exist a single node that shares the same length as the tube. During the simulation, various parameters such as pressure, temperature, and others are calculated for each node every second.

This model simulation typically takes an average of 100-140 seconds to complete in all cases. Once the flow reaches a stable state, the calculated parameters in each second start to yield identical results. Based on this data, the mean values for the parameters at the nodes are calculated. Results will be discussed in the next chapter.

The primary objective of this simulation was to study how different L/D ratios influence two-phase critical flow phenomena in the discharge tubes, emulating the steam generator tubes. By exploring these conditions, the aim to gain insights into the behaviour of fluids in such systems and understand the factors that impact critical flow.

6 C-flow test facility Apros simulation results and analysis

The analysis involves examining the figures that have been generated based on the data obtained from the simulations. These figures serve as visual representations of the fluid properties and further aid in understanding the behaviour of two-phase critical flow within the discharge tubes. The data obtained to the following figures are taken from the simulations at the period when the critical flow conditions reached stable conditions.

The critical mass flow rate of the mixture at the end of the discharge tubes for 13 mm and 17 mm discharge tubes are presented in Figure 36.

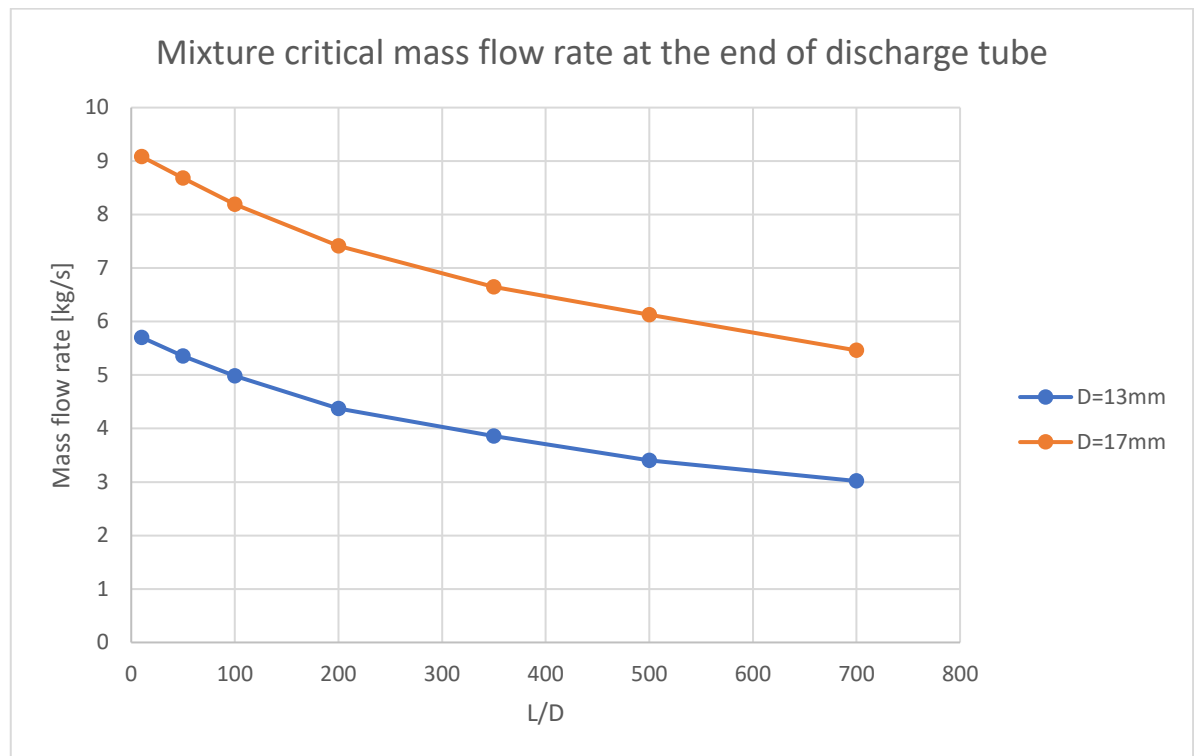


Figure 36: Mass flow rate at the end of discharge tube at 10 MPa pressure and 270 °C in vessel.

The results presented in this Figure 36 align with expectations based on the principles of fluid dynamics. As the L/D ratio increases, the wall friction increases because there is longer wall along which the flow has to slide. The larger diameter of the discharge tube allows for a greater flow area, resulting in a higher mass flow rate compared to the tube with a smaller diameter. The cross-sectional area of a tube is directly proportional to the square of the

diameter. Therefore, when the diameter of a tube increases, the flow area also increases, allowing more fluid to pass through per unit of time.

Figure 37 displays the critical mass flux as a function of the L/D ratio for two different tube diameters: 13 mm and 17 mm. The x-axis represents the L/D ratio, while the y-axis represents the critical mass flux.

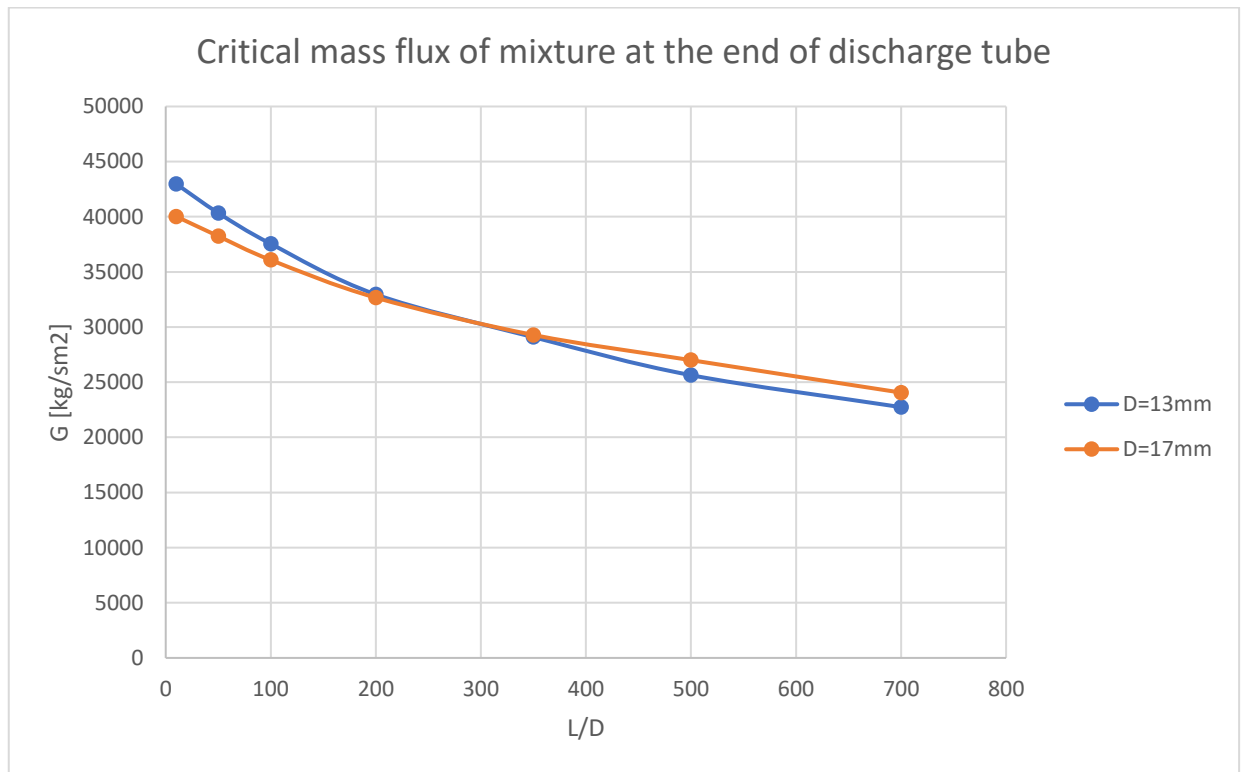


Figure 37: Critical mass flux at the end of discharge tube at 10 MPa pressure and 270 °C in vessel.

When the L/D ratio is small (e.g., L/D=10), it typically results in a more restricted and accelerated flow due to the relatively short flow path. This restriction can lead to higher critical mass flux values, as the flow rate approaches the choking condition for the given system. The tube diameter also plays a crucial role in determining the critical mass flux. A smaller tube diameter tends to promote higher critical mass flux, as it can create conditions where phase change (e.g., vaporization) occurs more readily.

As the L/D ratio increases, the flow regime and pressure drop become more influential in determining the critical mass flux. The decrease in critical mass flux with increasing L/D ratio suggests that the pressure drop along the tube becomes more significant. With higher L/D ratios, the pressure drop increases due to frictional losses and changes in flow regime,

which can limit the maximum achievable mass flow rate before reaching critical flow conditions. Figure 38 presents the pressure before the discharge tube as a function of the L/D ratio.

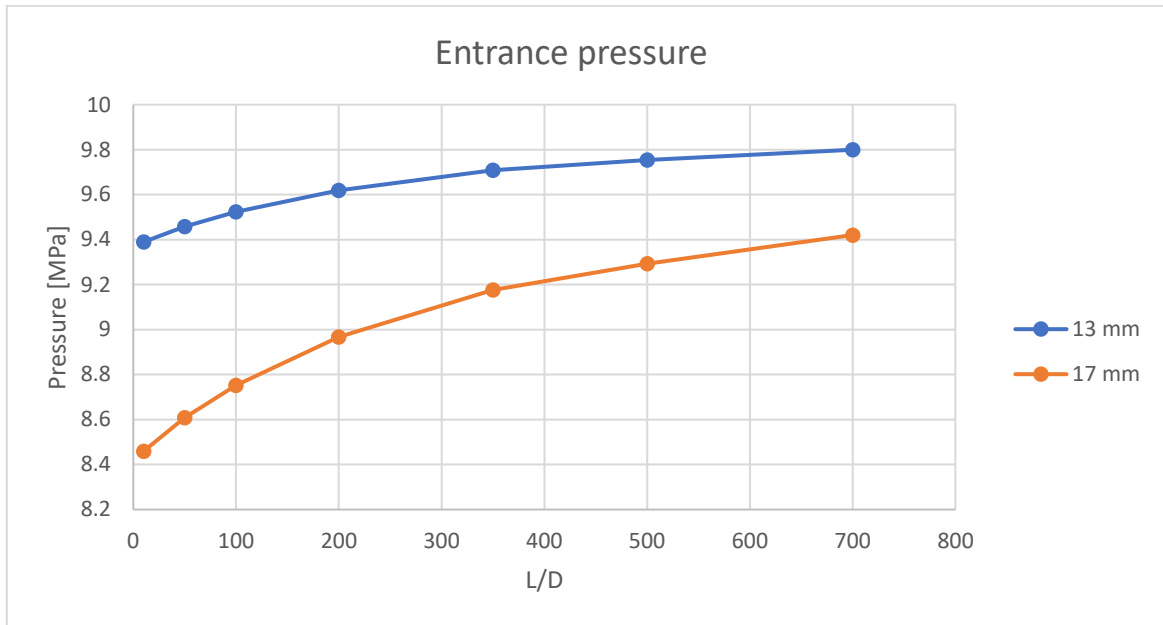


Figure 38: Pressure before discharge tube.

From Figure 38, can see the entrance pressure is lower in the 17mm diameter tube compared to the 13mm diameter tube. This discrepancy can be attributed to the higher mass flow rate associated with the 17 mm tube diameter. A larger diameter tube allows a larger mass flow rate through the system, resulting in a higher flow velocity in the U-tube. Consequently, the pressure drop before entering the discharge tube is higher for a 17 mm diameter tube. Furthermore, it is important to note that as the L/D ratio increases, the entrance pressure exhibits an upward trend for both tube diameters. This phenomenon is consistent with the decrease in mass flow rate as the L/D ratio increases

Figure 39 presents the pressure drop along the discharge tube and the void fraction at the end of discharge tube as a function of the L/D ratio for two different tube diameters.

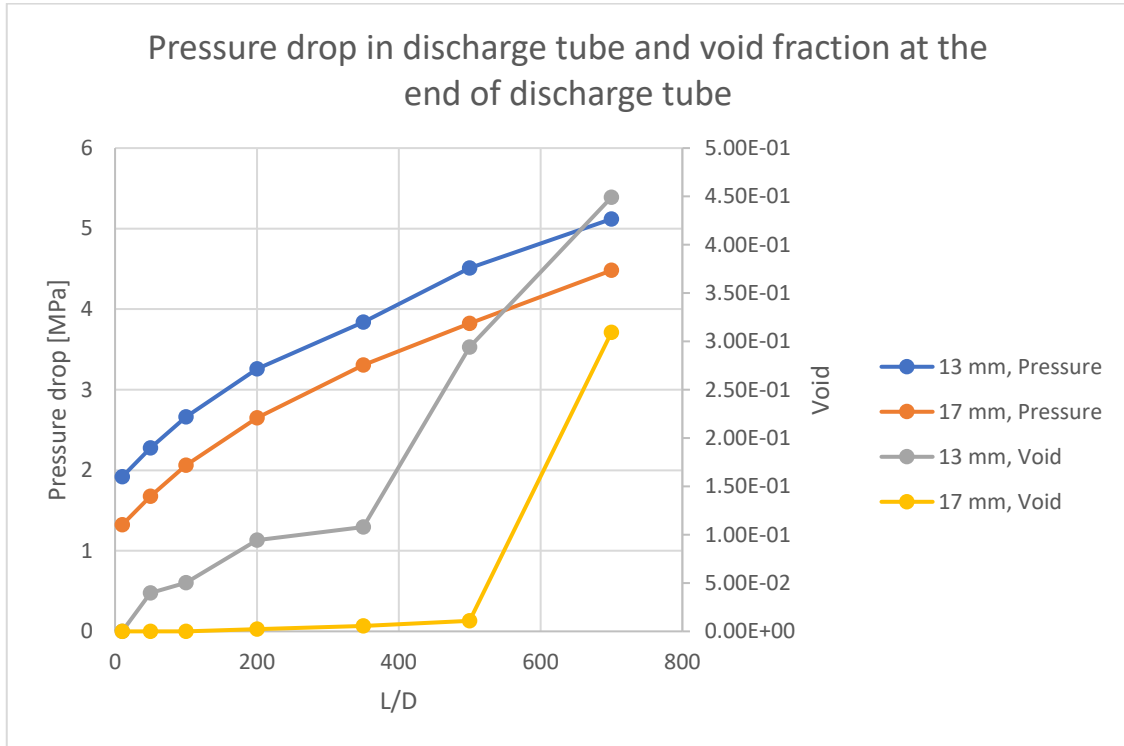


Figure 39: Pressure drop in discharge tube and void fraction at the end of discharge tube.

From Figure 39, it can be seen that the pressure drop in 13 mm diameter tube is consistently around 0.6 MPa up until it reach L/D higher than 200. And it is evident that the longer the tube, the larger the wall effects are and pressure drop increases. At the L/D 500 the pressure drop difference between two diameters cases are the highest due to large voiding in 13 mm diameter tube.

Figure 40 illustrates the relationship between the pressure at the end of the discharge tube and the L/D ratio.

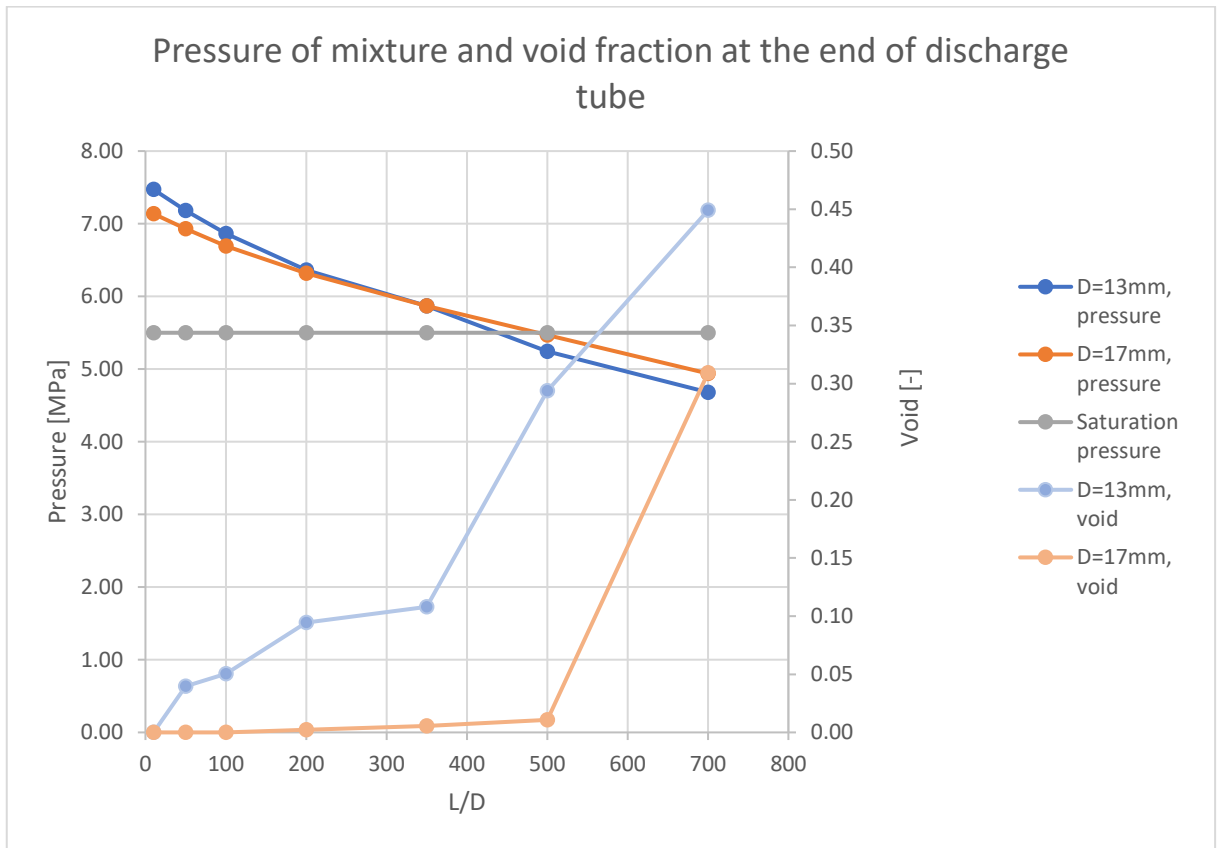


Figure 40: Pressure and void fraction at the end of discharge tube at 10 MPa pressure and 270 °C in vessel.

In Figure 37, the critical mass flux trends closely resemble to the pressure of the mixture observed in Figure 40. The high-pressure subcooled water enters the discharge tube and starts to undergo a pressure drop caused by the friction in the discharge tube's inner surface. Eventually with a large L/D ratio tube the pressure drops below the saturation pressure where voiding increases drastically compared voiding due to wall effects. The steam and saturated water will undergo interfacial mass and heat transfer which influence further pressure losses. During the flashing process, an additional pressure loss occurs mainly due to the expansion of the fluid volume as the liquid water transforms into steam as it reaches saturation pressure.

At higher L/D ratios around 500-700, the smaller diameter tube shows lower pressure at the end of the discharge tube compared to the tube with the larger diameter. This occurs because, as the L/D ratio increases, the mass flow rate through the system decreases, leading to a reduction in the pressure drop before the discharge tube and an increase in the entrance

pressure at the discharge tube. Furthermore, as the L/D ratio increases, the pressure drop within the discharge tube itself also increases, and this effect is more pronounced in smaller diameter tubes. Due to these interrelated factors, at lower L/D values, the pressure at the end of the discharge tube is higher for the 17 mm diameter tube. However, as the L/D ratio increases, this relationship undergoes a change. One of the reasons for the higher pressure drop in the smaller diameter tube, despite the greater frictional effects of the tube, is the higher void fraction observed in the 13 mm diameter tube compared to the 17 mm diameter tube at the end of the discharge tube. This increased void fraction can influence the pressure distribution and flow characteristics. As gas voids (bubbles) develop within the liquid phase, they result in a decrease in the overall density of the mixture. In response, the flow velocity tends to increase, driven by the need to maintain a constant mass flow rate. This change in flow velocity can affect the pressure drop along the tube.

Results show that for the 13 mm diameter tube, there is a significant increase in the void fraction as the L/D ratio increases. The higher pressure drop along the tube in the smaller diameter tube can promote flashing and result in an increased void fraction at lower L/D ratios. At an L/D ratio of 500, the void fraction reaches 0.30, and the flow reaches the saturation pressure, beyond which the formation of voids increases rapidly. Subsequently, at an L/D ratio of 700, the void fraction further increases to 0.45.

In contrast, for the 17 mm diameter tube, the void fraction remains low, nearly zero, until an L/D ratio of 500 at which point the flow reach saturation pressure. Beyond an L/D ratio of 500, the void fraction increases rapidly. Simultaneously, at this juncture, the mass flow rate decreases to levels similar to those observed in the 13 mm diameter tube at lower L/D ratios, resulting in a reduction in the liquid volume fraction. At an L/D ratio of 700, the void fraction reaches 0.30. However taking into account that the used nodelization may have an affect on void fraction value as results are taken as an average value of the last node.

In the larger diameter tube, the delayed increase in void fraction at L/D ratios from 10 to 500 can be attributed to several factors, including pressure drop, the larger flow area and higher mass flow rate, which allow for a slower expansion of gas bubbles and their separation from the liquid phase. The higher mass flow rate in the larger tube contributes to a greater liquid volume fraction, thus reducing the void fraction.

Figure 41 and Figure 42 present the velocity for liquid and gas as a function of the L/D ratio for two different tube diameters.

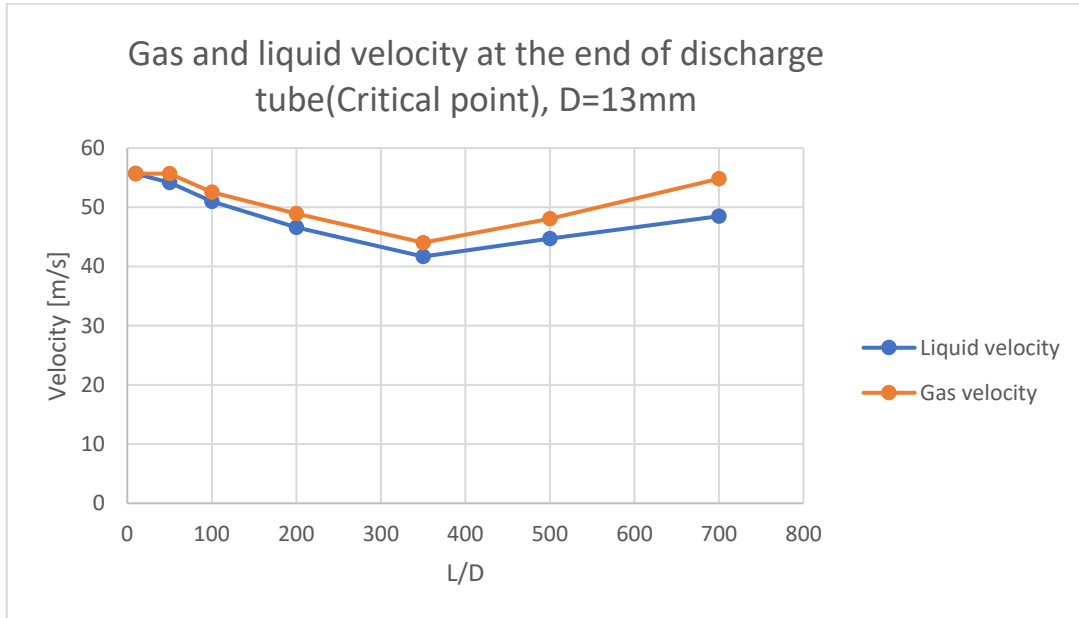


Figure 41: Gas and liquid velocity at the end of discharge tube.

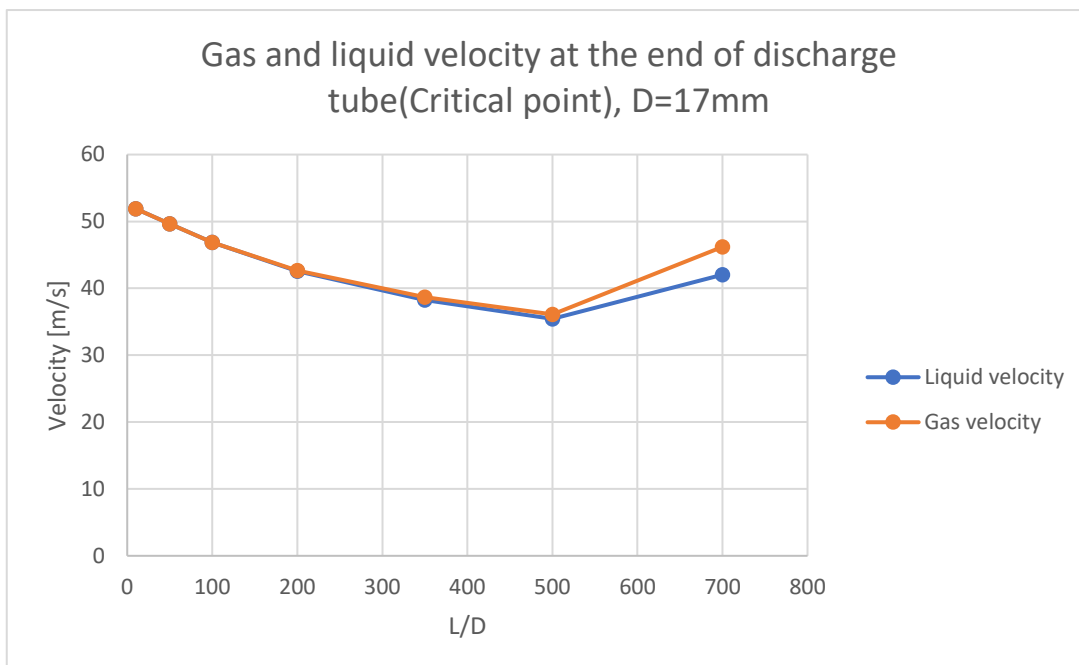


Figure 42: Gas and liquid velocity at the end of discharge tube.

The phenomenon where the velocity of both liquid and gas phases initially decreases with increasing L/D ratio and then starts to increase again, can be explained by the characteristics of two-phase flow and the effects of geometry on flow behaviour.

As L/D increase it can be seen that the velocity for both phases start to decrease. The length of the tubes increase, increasing the pressure drop, which lead to reduction in velocity. Also, as L/D increase the mass flow rate decrease, which also lead to decrease in velocity. At the point where flow reach saturation pressure it can be seen that velocity starts to increase for both phases. This is due to large increase in void fraction. For 13 mm diameter tube it is L/D's 350-500 and for 17 mm diameter tube it's start after L/D 500.

When the saturation pressure is reached, it means that the liquid is at its boiling point, and vaporization occurs. As the fluid changes from a liquid to a vapor, it expands and occupies a larger space. This expansion leads to a significant decrease in density. To maintain the same mass flow rate, the fluid particles have to move at a higher velocity. This increase in velocity is a result of the fluid particles spreading out over a larger area while simultaneously experiencing a reduction in density, all while maintaining their mass.

While there is an increase in the speed of the two-phase mixture, it's essential to understand that this increase in speed usually does not cause the velocities of either phase to approach the speed of sound.

Figure 43 and Figure 44 presents the void fraction as a function of the length of discharge tube for tube with diameter of 13 mm.

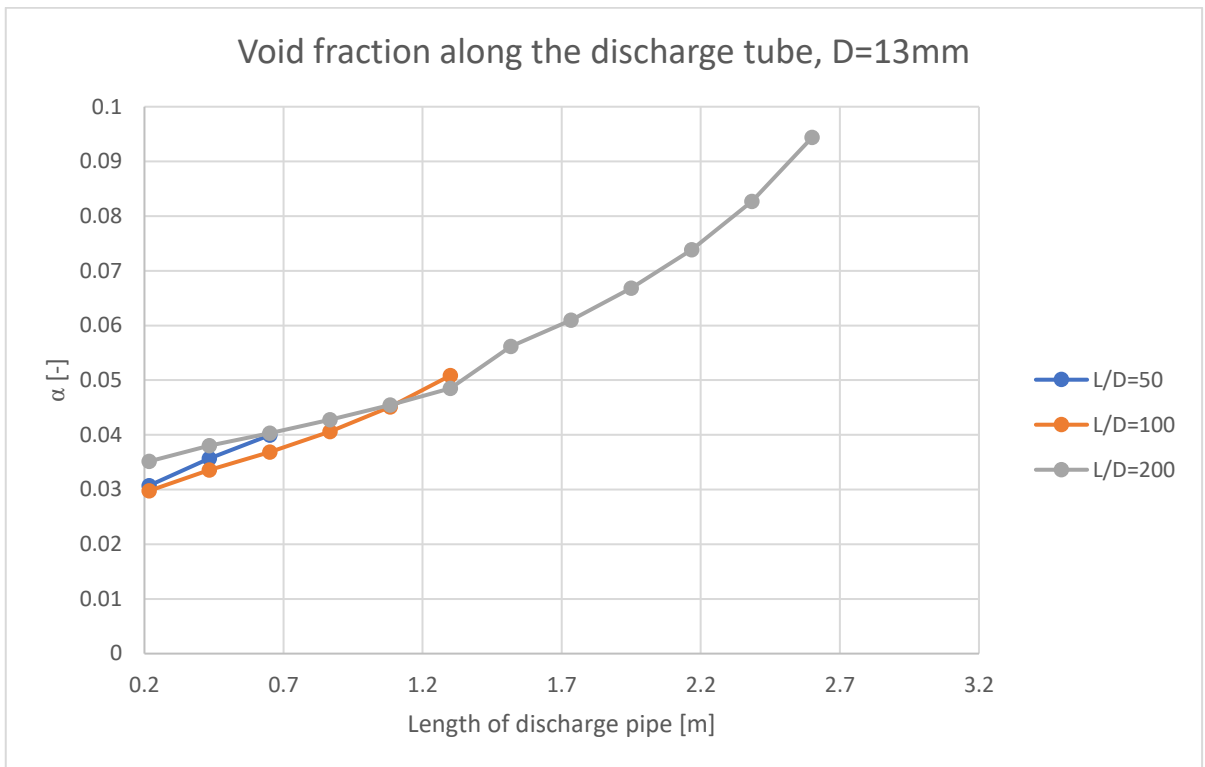


Figure 43: Void fraction along the discharge tube, D=13 mm

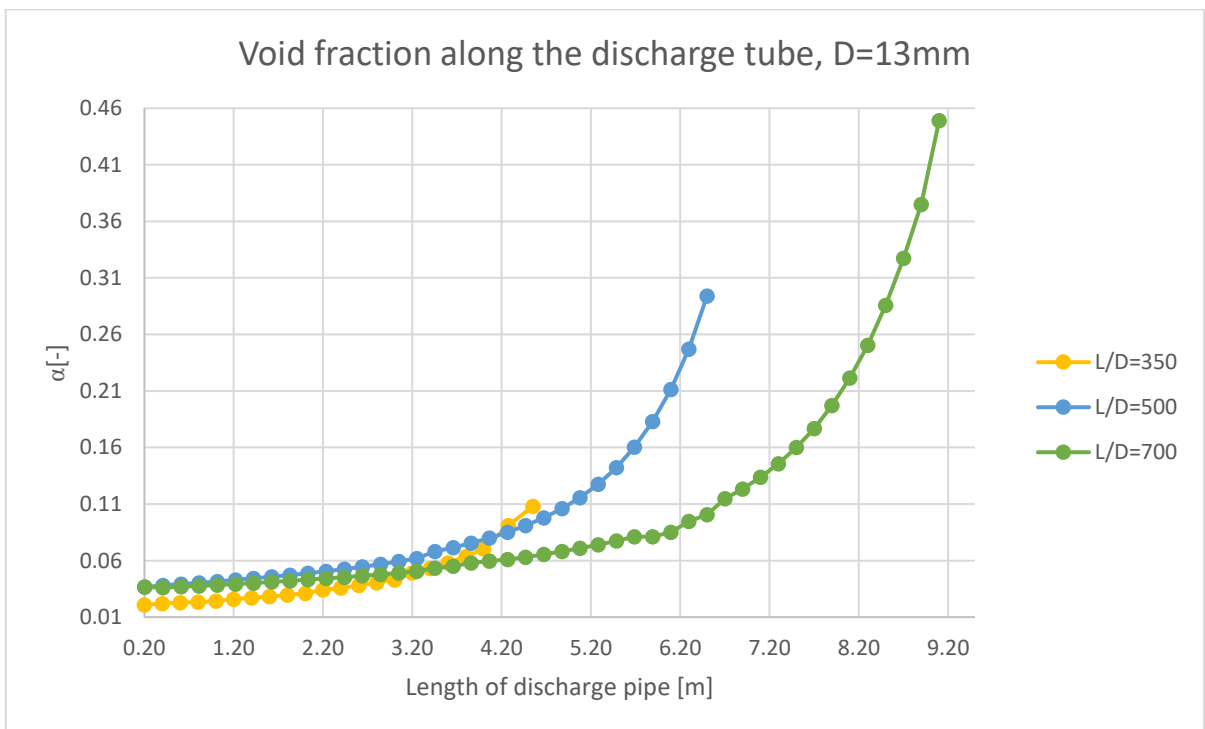


Figure 44: Void fraction along the discharge tube, D=13 mm

The Figure 43 illustrates a clear, linear increase in void fraction as the L/D ratio falls within the range of 50 to 200. With the increase of the L/D ratio, there is a concurrent rise in pressure drop within the tube, leading to a reduction in mass flow rate and, consequently, a diminished liquid volume fraction. These interrelated factors collectively contribute to a consistent and stable augmentation in void fraction along the length of the tube within this specified parameter range.

In cases where the L/D ratio extends to values between 350 and 700, an observable shift occurs, indicating an exponential rise in void fraction. This shift can be attributed to the reach of saturation pressure at the end of the discharge tube under simulation conditions. Increase in void fraction becomes more pronounced as it is closer to the end of discharge tube.

Figure 45, Figure 46 and Figure 47 present the void fraction as a function of the length of discharge tube for tube with diameter of 17 mm

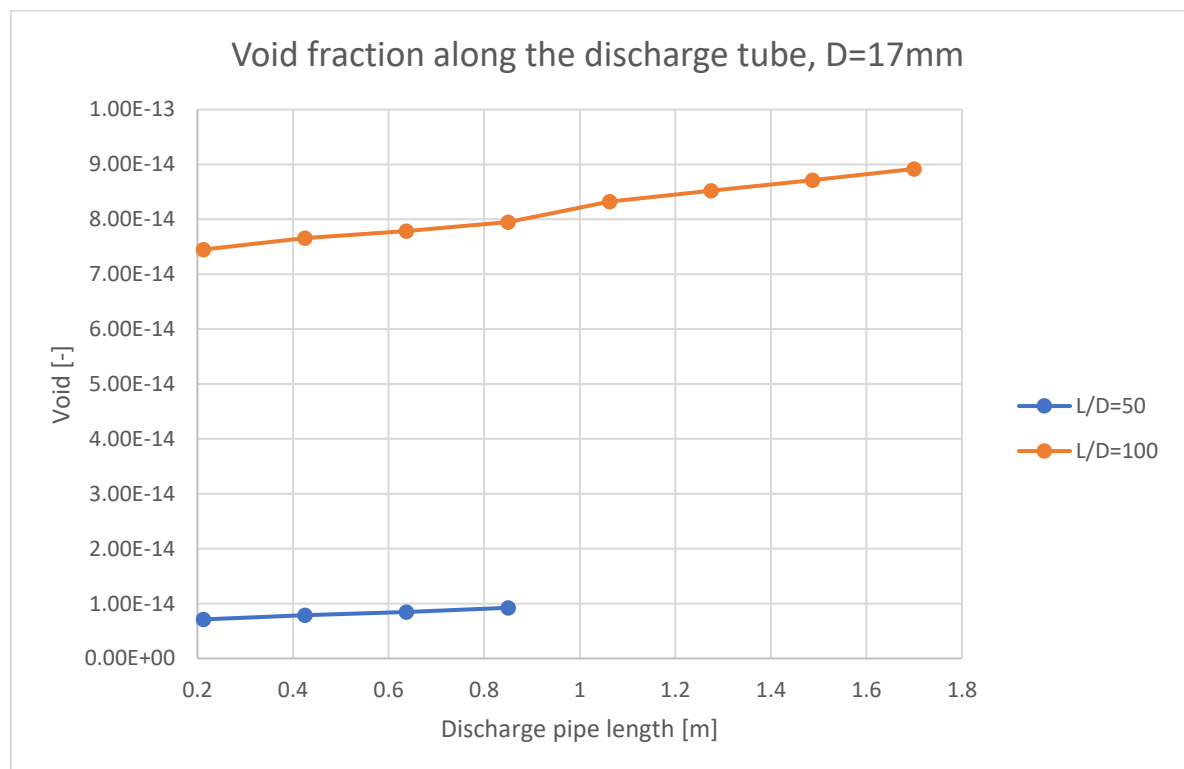


Figure 45: Void fraction along the discharge tube, D=17mm

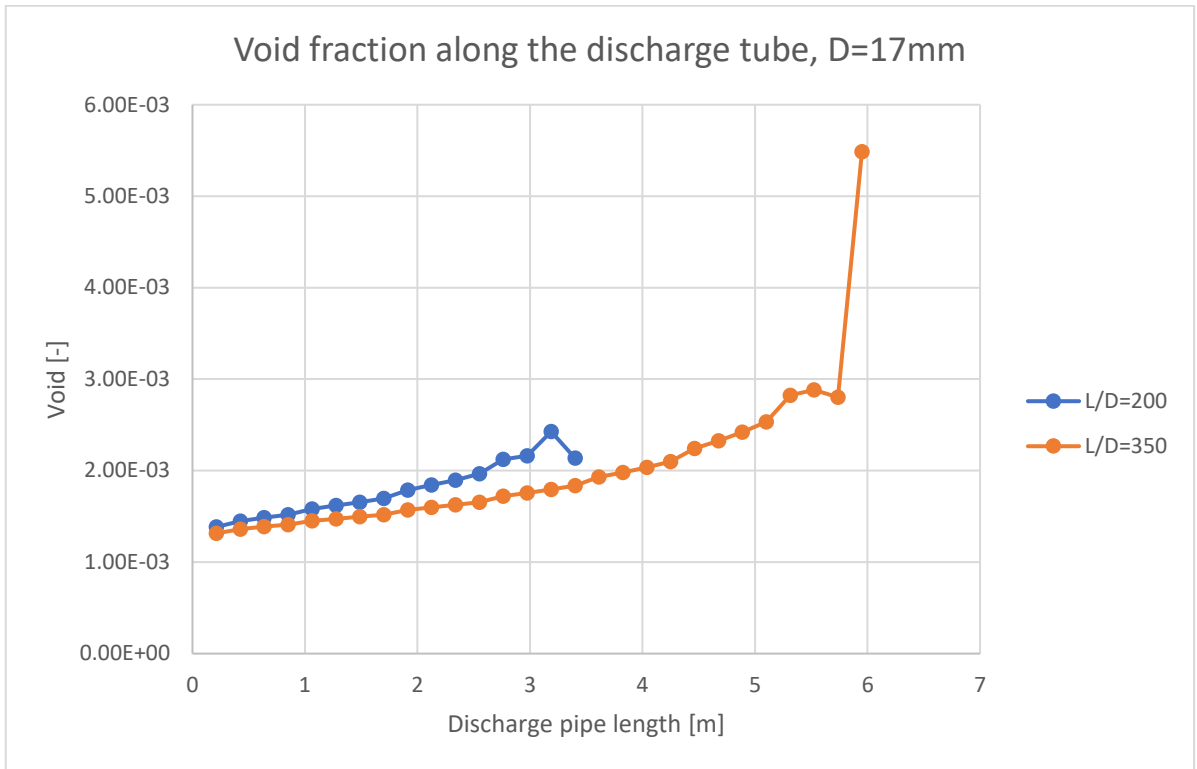


Figure 46: Void fraction along the discharge tube, D=17mm.

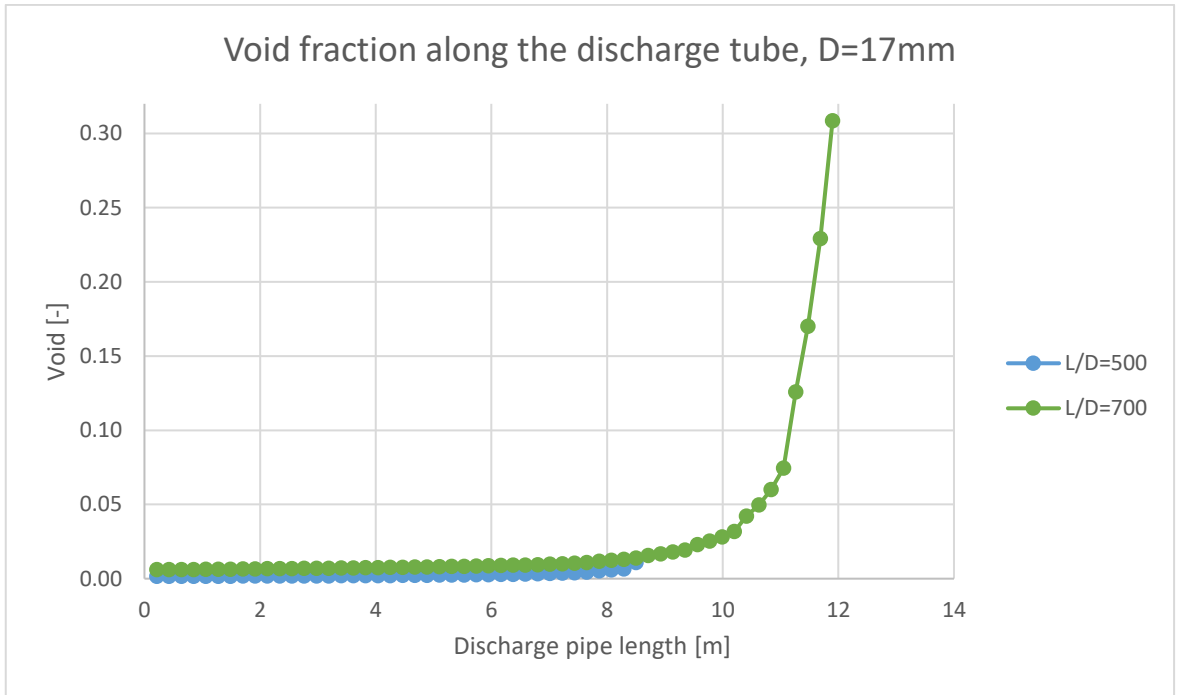


Figure 47: Void fraction along the discharge tube, D=17mm.

It is evident that the void fraction consistently maintains values in proximity to zero within the range of L/D ratios spanning from 50 to 350. It is noteworthy that the 17 mm diameter tube exhibits a notably higher mass flow rate. This phenomenon can be attributed to its enlarged cross-sectional area, thereby permitting a greater volumetric flow of water. The higher mass flow rate has an effect in sustaining a stable, predominantly liquid flow regime, minimizing the occurrence of significant void formation.

However, as the L/D ratios surpass 500 and escalate further, an exponential surge becomes apparent, notably when nearing the end of the tube. This phenomenon arises due to the fact that the saturation pressure is achieved. Consequently, this proximity to saturation pressure induces a rapid increase in void fraction.

7 Conclusion

This research is motivated by the necessity to gain a deeper understanding and predictive capabilities of critical flow phenomena in steam generator tube ruptures, ultimately enhancing safety and efficiency in nuclear power plant operations. The thesis aimed to develop a comprehensive model for simulating two-phase critical flow during a steam generator tube guillotine rupture scenario using Apros within the C-FLOW separate-effect-test facility.

The simulation results demonstrated the consistent achievement of criticality conditions at the end of the discharge tube for all tested cases. It was apparent that the L/D ratios of discharge tubes affected on critical flow behaviour. Notable variations were observed in fluid properties at the discharge tube outlet. Pressure, mass flow rate, void, and velocity of the liquid and gas phases exhibited distinct patterns based on the L/D ratio. Additionally, the analysis of void fraction along the tube provided insights into the evolution of two-phase flow regimes.

Through a comprehensive review of theoretical models, experimental studies, and simulation results, it was observed that there is no single generic critical flow model or correlation that applies universally to different pipe lengths, sizes, and upstream conditions. Different models have their limitations, especially for short pipelines or situations close to

liquid saturation or subcooled upstream. The consideration of thermal nonequilibrium for short pipelines is also necessary, although the specific influence of pipe length and length-to-diameter ratio requires further investigation.

The lack of a systematic scaling investigation for critical flow phenomena is highlighted, emphasizing the need for dimensionless analyses and the utilization of relevant dimensionless numbers to compare flow characteristics. By incorporating nondimensional groups representing numerous factors, a more comprehensive understanding of flow conditions and critical flow behaviour can be achieved.

The simulation results provided valuable insights into the effects of the L/D ratio on critical mass flow. Increasing the L/D ratio resulted in greater pressure drops and lower pressures at the discharge tube outlet due to frictional losses along the tube walls. The void fraction exhibited an increasing trend with the L/D ratio, indicating higher pressure losses and increased flow resistance, particularly for the smaller diameter tube.

Furthermore, the observations revealed the complex nature of two-phase flow. Initially, as the L/D ratio increases, the velocity for both liquid and gas phases tends to decrease. This reduction in velocity is influenced by factors such as the increasing pressure drop and the decreasing mass flow rate as the L/D ratio increases. When the fluid in the discharge tube reaches saturation pressure, it undergoes a phase change from liquid to vapor, resulting in a significant decrease in density. To maintain a constant mass flow rate, the fluid particles must move at higher velocities. This leads to an increase in velocity for both phases. This increase in velocity occurs as the fluid expands and occupies a larger space while experiencing reduced density.

To further enhance the capabilities of the test facility for conducting two-phase critical flow experiments, several upgrades could be considered. Upgrading the existing SCRAM tank or exploring alternative pressure vessels capable of handling higher pressures and temperatures is crucial.

As evident from the entrance pressure data, the 17 mm diameter tube, when operating at the lowest L/D ratio, exhibits an entrance pressure of approximately 8.4 MPa, while the 13 mm diameter tube registers a higher entrance pressure of around 9.4 MPa. It is noteworthy that as the L/D ratio increases, the entrance pressure correspondingly increase. To facilitate testing of discharge tubes with lower L/D ratios while maintaining higher entrance pressures,

it is imperative that the pressure vessel has the capacity to endure pressures within the range of 11.5-12 MPa. For the 17 mm diameter tube to maintain identical initial conditions before discharge tube as observed with the 13 mm diameter tube, the implementation of a control valve can be considered to adjust the mass flow rate to equivalent values.

A higher maximum pressure capacity, such as 15 MPa, would enable the investigation of critical flow under more realistic conditions, aligning with modern power plant operating conditions. Another possibility is to incorporate experimental setups or modifications to investigate thermal nonequilibrium effects during two-phase critical flow. Capturing temperature profiles along the discharge tubes will shed light on the influence of heat transfer phenomena, enhancing our understanding of critical flow behaviour and enabling improved thermal-hydraulic modelling.

Taking into account the significant differences in void fraction between the tubes, especially in the smaller L/D range, it could be beneficial to make simulations with computational fluid dynamics software to confirm the void fraction development in 17 mm diameter tube case. In future it would also be beneficial to investigate simulation cases, with different upstream conditions using thermal hydraulic system codes. As the simulation durations were relatively short increasing the amount of nodes and effect of that on the results could be investigated.

In summary, this thesis contributes to the understanding of critical flow phenomena in the context of a primary-to-secondary leak scenario in a separate-effect-test facility. The findings highlight the significance of considering the L/D ratio and tube diameter in predicting critical mass flow rates. The limitations of existing models, the need for further scaling investigations, and the complexities of two-phase flow dynamics provide opportunities for future research in this field.

References

- M.R. Nematollahi, A. Zare. 2008. A simulation of a steam generator tube rupture in a VVER-1000 plant. *Energy Conversion and Management*. Vol. 49. pp. 1972-1980.
- Revankar. S.T., Riznic, J., 2019, An experimental investigation of subcooled choked flow in actual steam generator tube cracks, *Nuclear Engineering and Design*. Vol. 354, pp.1-9.
- M. Lanfredini, D. Bestion, F. D'Auria , N. Aksan , P. Fillion , P. Gaillard , J. Heo , I. Karppinen , K.D. Kim , J. Kurki , L. Liu , A. Shen , J.-L. Vacher , D. Wang, 2020, Critical flow prediction by system codes – Recent analyses made within the FONESYS network, *Nuclear Engineering and Design*, Vol. 366, pp. 2-8.
- D.W.H. Fraser, A.H. Abdelmessih, 2002, A study of the effects of the location of flashing inception on maximum and minimum critical two-phase flow rates: Part I – experimental, *Nuclear Engineering and Design*, Vol. 211, pp. 1-11.
- P. E. MacDonald, V. N. Shah, L. W. Ward, P. G. Ellison, 1996, *Steam Generator Tube Failures*, Idaho National Engineering Laboratory, NUREG/CR-6365.
- Sokolowski L., Kozlowski T., Calvo A., 2012, *Assessment of Two-Phase Critical Flow Models Performance in RELAP5 and TRACE Against Marviken Critical Flow Tests*. International Agreement Report, Office of Nuclear Regulatory Research, U.S. Nuclear Regulatory Commission, Washington, DC 20555-0001.
- Kieffer S. W, 1977, Sound speed in liquid-gas mixtures: water-air and water-steam, *Journal of Geophysical Research (1896-1977)*, *Solid Earth and Planets*, 82(20), pp.2895-2904.
- Deych M.Y, Filipov G.A ,1969, *The Gas Dynamics of Two-Phase Media*, *Gazodynamika Dvukhfaznykh Sred*, Moscow.
- Kiestin J, 1991, Spurious solutions in critical two-phase flow numerical codes, In: *International Conference on Multiphase Flow*, Tsukuba, Japan.
- Rohatgi U.S., Reshotko E., 1975, Non-equilibrium one-dimensional two-phase flow in variable area channels, *ASME Conference Paper*, ASME, Houston, TX.

- D'Auria F., 2017, *Thermal-Hydraulics of Water-Cooled Nuclear Reactors*, Elsevier Ltd, University of Pisa, Italy, ISBN: 978-0-08-100679-5.
- Alamgir M.D., Lienhard J.H., 1981, Correlation of pressure undershoot during hot water depressurization, *J. Heat Transf.*, Vol.103, pp.522-525.
- Jones Jr. O.C., 1980, *Flashing Inception in Flowing Liquids*, Brookhaven National Laboratory Report BNL-NUREG-51221, also NUREG/CR-1515.
- Ritcher H.J., 1983, Separated two phase flow model: application to critical two-phase flow, *Int. J. Multiphase Flow*, Vol.9, no.5, pp.511-530.
- Moody F.J., 1965, Maximum flow rate of a single component, two-phase mixture. *Trans. A.S.M.E. Series C., J. Heat Transfer*, Vol.87, pp.134-142.
- Moody F.J., 1966, Maximum two-phase vessel blowdown from pipes, *J. Heat Transf.*, Vol.87, pp.285-295.
- Henry R.E., Fauske H.K., 1971, The two-phase critical flow of one-component mixture in nozzle. orifices and short tubes, *Trans. A.S.M.E. Series C., J. Heat Transfer*, Vol.93, pp.179-187.
- Henry R.E., 1970, The two-phase critical discharge of initially saturated or subcooled liquid, *Nucl. Sci. Eng.*, Vol.41, pp. 336-342.
- Fauske H.K., 1962, *Contribution to the Theory of Two-Phase One Component Critical Flow*, Argonne National Laboratory Report, ANL-6633.
- Henry R.E., Fauske H.K., McComas S.T., 1970. Two-phase critical flow at low qualities, partII, *Nucl. Sci. Eng.*, Vol.41, pp. 92-98.
- Saha, P., 1978, *A Review of Two-Phase Steam-Water Critical Flow Models With Emphasis on Thermal Non-equilibrium*, NUREG/CR-0417, Washington. DC: US Nuclear Regulatory Commission.
- Elias E., Lellouche J., 1994, Two-phase critical flow, *Int. J. Multiphase Flow*, Vol.20, pp.91-168.
- Levy S., 1999, *Two-Phase Flow in Complex Systems*, John Wiley & Sons, New York.

Brittain I., Karwat H., D'Auria F., Vigni P., Hall D.G. & Reocreux M., 1982, Critical Flow Modelling in Nuclear Safety, NEA/OECD, Paris, ISBN 92-64-12366-0.

Miller J., 2010, Fundamental of nuclear engineering-module 13. available: <http://www.nre.gov/does/MLI214/ML12142A162.paf>.

OECD/NEA/CSNI, 1980, Two Phase Critical Flow Models, CSNI 49, Paris.

OECD/NEA/CSNI, 1993. A separate effects test matrix for thermal-hydraulic code validation: phenomena characterization and selection of facilities and tests, OECD/GD (94) 82, Vol. I&II, Paris, France.

Aksan, N. et al., 1994, OECD/NEA-CSNI Separate Effects Test Matrix for Thermal-Hydraulic Code Validation.

Lanfredini M., Lutsanych S, 2020, FO-02 Critical Flow Benchmark, FONESYS Report, Rev. 5, Pisa, Italy.

Riegel, B., 1978, Contribution à l'étude de la décompression d'une capacité en régime diphasique, Ph.D. thesis, Université Scientifique et Médicale et Institut National Polytechnique de Grenoble, France.

Edwards A.R., O'Brien F.P., 1970, Studies of phenomena connected with the depressurization of water reactors, J. British Nucl. Energy Soc. Vol.9, pp.125–135.

Attou A., Bolle L., Seynhaeve J.-M., 2000, Experimental study of the critical flashing flow through a relief line: evidence of the double-choked flow phenomenon, Int. J. Multiphase Flow, Vol.26, no. 6, pp.921–947

Sekri A., 1982, Cinétique d'ébullition de l'eau en décompression rapide, Ph.D. thesis, Louis Pasteur University, Strasbourg, France.

Sozzi G.L., Sutherland W.A., 1975, Critical flow of saturated and subcooled water at high pressure, Core and safety development NEDO-13418, Nuclear Energy Division, General Electric Company, California, USA.

Abuaf N., Wu B.J.C., Zimmer G.A., Saha P., 1981, Study of non-equilibrium flashing of water in a converging-diverging nozzle, Volume 1: Experimental, Volume 2: Modeling, NUREG/CR-1864, BNL-NUREG-51317, USA.

U.S. Nuclear Regulatory Commission, TRACE V5.0 Assessment Manual: Appendix B Separate Effects Tests, Division of Risk Assessment and Special Projects, Office of Nuclear Regulatory Research, Washington, DC.

Hall D. G., Ericson L, 1979, THE MARVIKEN CRITICAL FLOW TESTS: A DESCRIPTION AND EARLY RESULTS, Marviken CFT Project, Marviken, Sweden.

U.S. Nuclear Regulatory Commission, Forsøgsanlæg Risø., Marviken Power Station, 1982, The Marviken full scale critical flow tests: summary report: joint reactor safety experiments in the Marviken Power Station Sweden, Washington, D.C.: The Commission: GPO Sales Program, Division of Technical Information and Document Control, U.S. Nuclear Regulatory Commission; Springfield, Va.: National Technical Information Service.

Karppinen, I, 2016, Assessment of Apros thermal hydraulic models with separate effect tests, Research Report, VTT-R-06020-15.

Park H-S., Choi N-H., Chang S-K., Chung C-H., Yi S-J., Park C-K., Chung M-K, 2007, Experimental study on a two-phase critical flow with a non-condensable gas at high pressure conditions, International Journal of Multiphase Flow, Vol.33, pp.1222-1236.

Xu J., Wang R., 1999, Critical flow with high pressure water flowing in small diameter sharp-edged tubes, Heat and Mass Transfer, Vol.35, pp.205-220.

Heckmann K., Silber F., Sievers J., Stumpfrock, L., Weihe S., 2022, A metastable jet model for leaks in steam generator tubes, Nuclear Engineering and Design, Vol.389, 111673.

Schmid S., Silber F.E., Heckmann K., Kulenovic R., Laurien E., Sievers J., Weihe S, 2021. Leak rate testing in the range of leak detection systems, Nuclear Engineering and Design, Vol.372, 111000.

Bestion et al., 2023, Recommendations for new Experiments able to better Characterize Flashing Flows in nozzles for improving Critical Flow Modelling in System Codes, NURETH-20 article draft.

Kim S-M., Mudawar I., 2015, Review of two-phase critical flow models and investigation of the relationship between choking. premature CHF. and CHF in micro-channel heat sinks, International Journal of Heat and Mass Transfer, Vol.87, pp.497-511.

Hänninen. M, Ylijoki. J, 2008, The one-dimensional separate two-phase flow model of Apros, Espoo: VTT, ISBN 978-951-38-7224-3 (nid.), Number 2443.

Kurki. J, Ylijoki. J, Leskinen. J, 2019. Apros version 6.09, The Constitutive Equations of the Two-Fluid Model, Reference manuals, Thermal hydraulics, Flow model 6, Constitutive equations. VTT Technical Research Centre of Finland

TVO, 2010. Nuclear Power Plant Unit Olkiluoto 3, Eurajoki: TV.